공학박사 학위논문

Measurement for *in-vivo* bio samples using miniaturized THz endoscope

소형화된 THz 내시경을 이용한 *in-vivo* 생체 측정에 관한 연구

지도교수 전 태 인

2013년 2월

한국해양대학교 대학원

전기전자공학과

지 영 빈

공학박사 학위논문

Measurement for *in-vivo* bio samples using miniaturized THz endoscope

소형화된 THz 내시경을 이용한 *in-vivo* 생체 측정에 관한 연구

지도교수 전 태 인

2013년 2월

한국해양대학교 대학원

전기전자공학과

지 영 빈

본 논문을 지영빈의 공학박사 학위논문으로 인준함.

위원장 서 동 환 (인)

위 원 전 태 인 (인)

위 원 장 낙 원 (인)

위 원 주 양 익 (인)

위 원 오 승 재 (인)

2012년 12월 14일

한국해양대학교 대학원

Table of contents

List of figures

Figure

Figure

Figure

Figure

List of Tables

Table

소형화된 THz 내시경을 이용한 *in-vivo* 생체 측정에 관한 연구

지영빈

한국해양대학교 전기 전자 공학부
공과 대학원

요약문

21세기를 맞이하여 의학의 눈부신 발달로 사람들의 평균수명이 점점 연장되면서 현대의 사람들은 건강히 오래 사는 방법에 많은 관심을 가지고 있다. 생명과 관련한 대부분의 중대한 질병의 경우, 질병의 조기 발견이 치료에 있어 매우 중요한 요인이 된다. 중대한 질병들 가운데 암은 특히, 그 질병의 조기 발견이 매우 중요한 질병중의 하나이며 조기 진단을 하였을 경우 생존율이 매우 높아진다.

본 논문에서 암식별에 뛰어난 광섬유가 결합된 테라헤르츠 (THz) 내시경을 설계, 제작하고 그 특성에 대해서 보고하였다. 광섬유를 이용하여 펨토초 레이저를 유도하였으며 광전도 방식을 사용하여 THz파를 발생하고 검출하였다. 반사된 THz파를 측정하였을 때 전통적인 THz 분광학에서 측정된 신호와 거의 유사한 신호 대 잡음비와 스펙트럼을 얻었다. 제작된 THz 내시경의 크기는 (2mm

X 4mm) X 6mm로 사람의 몸에 삽입할 수 있을 정도로 소형화 되었다. 제작된 THz 내시경이 실제 응용 분야에 적용이 가능함을 확인하기 위하여 기존에는 측정할 수 없었던 입안 벽 세포와 혀, 손바닥, 물에 반사된 THz파를 측정하여 그 결과를 비교하였다. 입안 벽과 혀에서 반사된 신호는 물에서 반사된 신호와 유사한 결과를 나타내었으며 손바닥에서 반사된 신호는 지방의 함유량이 많아서 나머지 결과들과 구분되는 신호를 나타내었다. 실험 결과로부터 제작된 THz 내시경이 서로 다른 생체를 구분할 수 있음을 보였으며 이는 제작된 내시경이 사람 몸에 삽입되어 충분히 암을 식별할 수 있음을 간접적으로 보였다.

THz 내시경 외에 기존의 검이경과 결합하여 중이염을 객관적으로 진단할 수 있는 또 하나의 의료 진단 장치인 THz 검이경을 설계, 제작하여 연구하였다. THz파는 수분과 쉽게 상호 작용하여 유생 분자 내에 있는 물의 함유량을 구분할 수 있다. 중이염의 대부분은 물과 고름으로 이루어져 있고 따라서 제작된 THz 검이경으로 고막의 뒤에 있는 수분을 측정함으로써 기존의 의사의 임상적 경험과 광학적인 방법으로 진단하던 중이염을 객관적인 측정결과에 기초하여 정확히 진단할 수 있음을 보였다. 실제 고막을 모델링한 유전체 박막과 쥐 피부를 이용하여 시뮬레이션과 실험을 진행하였으며 그 결과들로 제작된 THz 검이경이 중이염을 진단할 수 있음을 증명하였다.

THz 파의 생체 의학(bio-medical) 분야로서의 잠재력은 늘 인정 받아왔으나 실제 의료 현장에 적용 가능한 THz 의료장치는 거의 없었다고 할 수 있다. 본 논문은 실제 의료현장에 적용이 가능할 만큼 뛰어난 THz 의료 장치를 개발 하였고 특히 THz 검이경은 2017년 안에 상용화가 가능할 것으로 기대되며 상용화될 경우 매우 큰 파급력이 있을 것으로 예상된다.

1. Introduction

People are currently paying much attention to how they can live long and healthy lives through the development of medical science. Early diagnosis of serious diseases is extremely important for treatment, and various medical imaging devices and diagnostic apparatuses that can achieve early diagnosis have been developed rapidly. Typical medical imaging devices such as magnetic resonance imaging (MRI), computed tomography (CT), positron emission tomography (PET), and ultrasonography are widely used.

Cancer is a serious disease whose early diagnosis is especially important for treatment. If the early cancer diagnosis is achieved, the survival rate for patients is extremely high. According to the ‘Investigation of Cancer Rate in 2009’ by the National Cancer Center in Korea, digestive cancers, including gastric cancer, colon cancer, and liver cancer, have the highest rates of occurrence in Korea (40%). The early diagnosis and treatment of digestive cancers is most important, because anti-cancer drug treatments are not effective for digestive cancers, and resistance to chemotherapeutic agents occurs more often with digestive cancers compared with other carcinomas.

The MRI technique has some problems in diagnosis involving digestive organs and skin, in that the spatial resolution is limited to several millimeters. The high-energy of CT techniques can injure the human body, and the CT technique has difficulty distinguishing between cancer and normal tissue in soft tissues like digestive organs. The PET technique has insufficient spatial resolution to distinguish the boundary between cancer and normal tissue. Existing medical imaging devices are limited to in-situ diagnosis for digestive organ carcinomas such as gastric cancer, so complementary, alternative, and novel devices which are patient-friendly with excellent accessibility are needed.

Reliable candidates for new diagnostic devices include apparatuses that use terahertz electromagnetic waves (THz waves). THz waves lie in the frequency range of from 0.1 THz to 10 THz (with corresponding energy of 0.41~41 meV), as shown in figure 1-1. THz time-domain spectroscopy (THz-TDS) is a typical application of THz wave technology, and provides information of amplitude and phase, which can reveal the unique properties of materials, such as the refractive index, power absorption, and complex conductivity. THz waves have superior performance for distinguishing materials by providing a unique form of the resonant frequency, like a finger print, which is provided from interactions with intramolecular and intermolecular vibration, as well as the rotation of molecules [1-5].

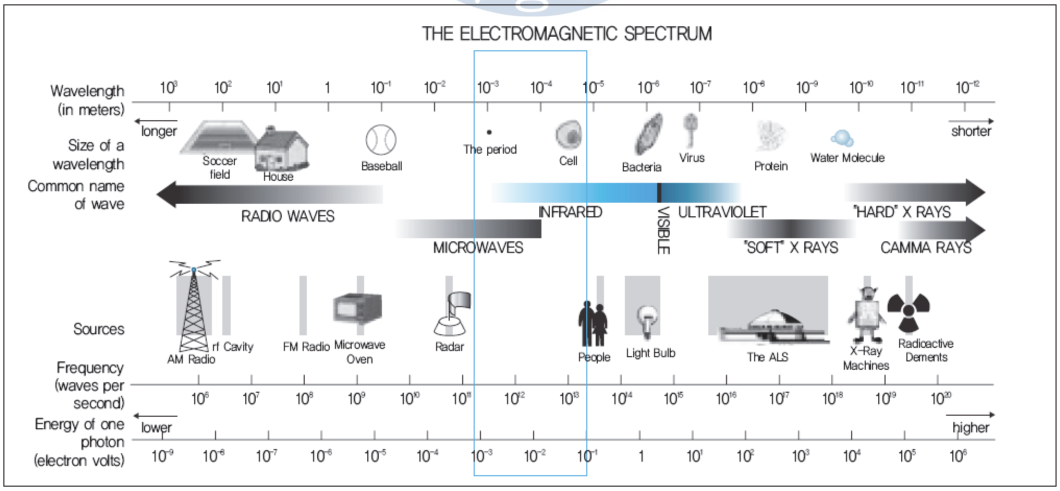

Figure 2-1. Spectrum of electromagnetic waves

Tissue or bio-medical material is mostly filled with water or liquid, and because THz waves are very sensitive to water content and bio-material structural changes, THz wave techniques have tremendous potential in the medical imaging field and in the study of biological materials. In contrast with CT techniques, THz waves are currently known as harmless to the human body due to their low energy [6-7]. The spatial resolution of THz imaging is less than 100 um, which is more than 10 times better performance compared to MRI and PET [8-9]. For this reason, from the end of the 20th century until now, the applications of THz waves for bio-medical research have been increasing rapidly and attracting interest from many researchers around the world. THz spectroscopy has been used to investigate a variety of biological molecules, including DNA [10], RNA [11], and protein [12]. In particular, numerous studies related to cancer diagnosis have been carried out [13-15]. As mentioned above, THz waves sensitively interact with water molecules. Cancer cells grow rapidly because of rapid cell division, and the water content differs between normal tissue and cancer cells. This is caused by the different numbers of cells and different water contents between cells, which enables the diagnosis of cancer using THz waves.

However, there is difficulty distinguishing between general inflamed cells and cancer cells, because the water content of general inflamed cells also differs from that of normal tissue, as a result the similar THz measurements. Various studies have been carried out in order to overcome this disadvantage. For example, one such study used gold nanorods (GNRs) [16].

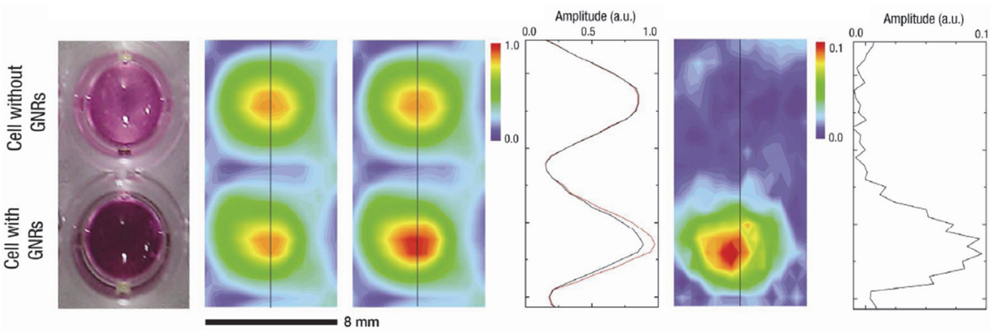

Figure 1-2 Cancer diagnosis using GNRs [16].

GNRs can be injected into a specific organ or cancer, and heat is generated when a laser beam irradiates the GNRs, due to resonant vibration. The reflected THz waves from laser-irradiated cancer cells with or without GNRs are distinguished, and we can explicitly diagnose either cancer cells or normal tissue, as shown in figure 1-2.

The conventional THz systems used in bio-medical research, like that shown in figure 1-3, have been fixed and bulky. Because the systems are fixed, most bio experiments have only been carried out ex-vivo and in-vitro,

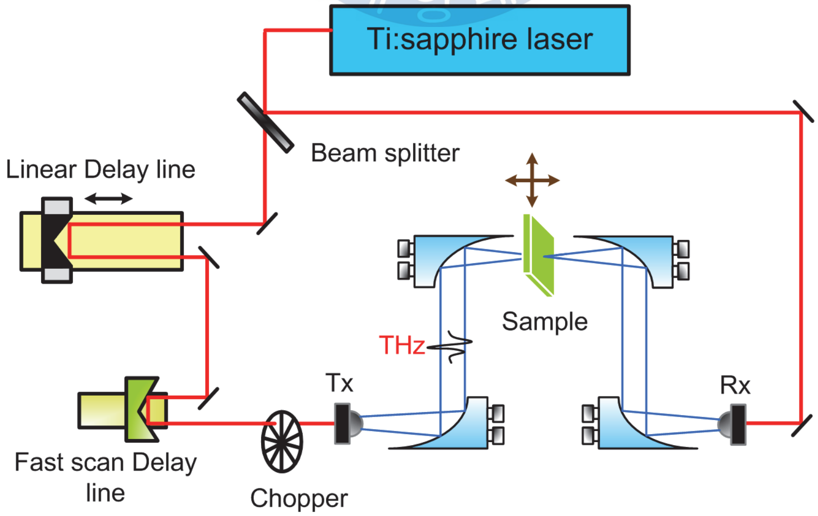

Figure 1-3 Traditional THz TDS system

with THz waves for THz imaging being measured by moving the sample. Measurements of a few in-vivo bio samples from the human body, such as the palm of hand, have been restrictively carried out due to the fixed nature of conventional THz systems [17].

In order to overcome these disadvantages and limitations, and to extend the versatility of THz-based diagnostic systems to internal organs, an endoscope should be developed to measure THz waves in limited spaces such as the stomach after passing through the esophagus or colon. In order to manufacture a THz endoscope (TES), a waveguide that can guide THz waves freely like optical fiber is essential. Extensive research is being done to develop efficient THz-frequency waveguides. The propagation of THz waves has been studied in circular metal tubes [18], rectangular metal tubes [19], high-density plastic ribbons [20], parallel plate metal waveguides [21], copper coaxial cables [22], single-metal wire [23], and twin-metal wire waveguides [24] etc. However, these waveguides are not practical for TESs, because they suffer from considerable signal distortion or large absorption at the small bends of the waveguide.

A realistic alternative is to generate and detect THz signals near the reflective surface of an organ by femtosecond lasers guided through optical fibers. Recently, fiber-coupled THz-TDS systems[25–27] were reported, but these were too large to be applied as an endoscope. In order to apply fiber-coupled THz-TDS techniques to an endoscope, miniaturizing the THz transmitter (Tx) and receiver (Rx) modules is necessary.

Another serious drawback of conventional THz systems for bio-medical applications is slow measuring time. This drawback has been overcome by a variety of high-speed scanning methods that have been developed in recent years, such as asynchronous optical sampling (ASOPS) [28], electronically controlled optical sampling (ECOPS) [29-30], and rotary optical delay lines (RODL) [31].

In the past 10 years, there have been many studies about the potential of THz waves for bio-medical applications. However, practical THz medical devices have not been used in the actual medical field due to the aforementioned drawbacks. The only commercialized medical device using THz waves is manufactured by Teraview [16].

The properties and manufacturing processes of practical THz medical diagnostic devices that can be commercialized are reported herein. Novel THz medical devices are miniaturized and combined with high-speed scanning methods, and the devices can consequently measure and analyze bio-samples such as the stomach and colon, which cannot be measured using THz waves.

In Chapter 2, fiber-coupled THz-TDS technologies are introduced, and the manufacturing processes prototype of a THz endoscope (PTES) with integrated components are described in detail.

In Chapter 3, the manufacturing processes of a miniaturized THz endoscope (MTES) are described, and the propagation properties of THz waves emitted from an MTES are investigated. The in-vivo measurement of parts of the human body such as the side wall of the mouth and the tongue, which cannot be measured using THz waves are also reported.

In Chapter 4, the manufacturing methods of a super miniaturized THz Endoscope (SMTES) are proposed. A transceiver, which comprises Tx and Rx modules, is used in this method to can reduce the size compared to MTES. In addition, the possibility of manufacturing a new SMTES using the photo-Dember effect is reported.

In Chapter 5, the manufacturing processes of a THz otoscope (TOS), another practical medical diagnostic device, are described. A TOS can diagnose otitis media objectively. It is demonstrated that the TOS can diagnose otitis media through experimental and simulation results of a dielectric thin film and mouse skin, which are modeled as a tympanic membrane. A conclusion is presented in Chapter 6.

2. Prototype THz endoscope for modularization with fiber-coupled THz system

2.1 Experimental setup for fiber-coupled THz endoscope system

As mentioned Chapter 1, THz waves have infinite potential for bio-medical applications, but there are limitations in practical application by the fixed and bulky nature of the conventional THz-TDS system. Endoscopes have been widely used for in-vivo measurements of the human body due to their exceptional versatility and practicality. Development of TESs can reduce time for the diagnosis of cancer by biopsy and can considerably reduce costs by THz technology. The developed TES also will contribute to increase the survival rate of cancer patients by the early diagnosis of cancers.

A THz waveguide that can move freely and have no signal distortion and absorption should be developed for TESs. Various THz waveguides have been studied by many reserachers thus far, but there is no THz waveguide to apply to the TES. The fiber-coupled THz-TDS technique was introduced by S. A. Crooker in 2002 [26]. In order to develop the TES for bio-medical applications, using a fiber-coupled THz system is one possible approach.

2.1.1 THz generation with photoconductive method

THz pulses have widely been generated by photoconductive, optical rectification, and surface emission methods. The photoconductive method has been used for TESs. Laser pulses are used to generate THz waves from a Ti:sapphire mode-locked laser with durations of approximately 60 fs at a repetition rate of 83 MHz. The center wavelength of the pulses is 780 nm. Generally, the simple coplanar transmission line structure of a Tx chip consists of two 10-µm-wide metal lines separated by 80 µm and fabricated on semi-insulating (SI) GaAs, which has high dark resistivity and high carrier mobility. As the laser pulses arrive at the antenna of the Tx chip, holes and electrons are generated, because the energy of the 780-nm laser beam (1.59 eV) is greater than that of the GaAs band gap. After that, the DC bias voltage on the order of 10^6 V/m is applied to the Tx antenna. The generated carriers are immediately accelerated by the applied electric field, a resulting transient photocurrent flows, and a dipole moment is formed in the substrate. Finally, a THz wave which proportional to Maxwell’s equation ($E(t)\ \alpha\ \partial J(t)/\partial t$) radiates to free space. The radiated THz wave is collimated by a high-resistivity silicon (Si) lens. The refractive index of GaAs is 3.595 at 1 THz [32], and that of Si is 3.417 in the THz frequency regime. The difference in refractive indices is small, so the Fresnel reflection is very low. Consequently, most of the THz waves radiate well to free space without any losses. The principles of THz wave generation are described in detail in the reference [33].

2.1.2 THz detection with photoconductive method

The THz pulses have widely been detected using electro-optical sampling methods and photoconductive sampling methods. The photoconductive sampling method has been used for TESs. In the reverse processes of photoconductive generation, propagated THz pulses through free space are focused by a high-resistivity Si lens onto the Rx antenna on low-temperature-grown (LTG) GaAs substrate. Generally, a 20-µm-wide dipole antenna structure with a 5-µm gap is embedded in a coplanar transmission line consisting of two parallel 10-µm-wide lines separated from each other by 30 µm. As the propagated THz pulses and detection laser pulses arrive at the Rx dipole antenna at the same time, the generated carriers by the laser pulses are accelerated by the electric field of the THz pulses. The resulting transient photocurrent flows on the Rx dipole antenna and is finally measured by a low-noise amplifier and lock-in amplifier. The LTG GaAs substrate has high dark resistivity ($>10^7$MΩ) and short carrier lifetime (<550fs). The lock-in amplifier is used to measure the photocurrent, which is very small, on the order of nA or pA. The lock-in amplifier (also known as a phase-sensitive detector) is a type of amplifier that can extract a signal from noise using a reference signal. There are 3 methods to provide a reference signal to the lock-in amplifier. The first is the method of chopping THz waves using an optical chopper, the second involves chopping the Tx laser beam using an optical chopper, and the third involves using an AC bias voltage. In this study, reference signals are applied by a suitable method depending on the experimental environment.

2.1.3 Laser pulse dispersion and related THz signal

The femtosecond (10^{-15}) laser pulses used to generate THz waves are one of the very important factors in the measurement of THz waves. The

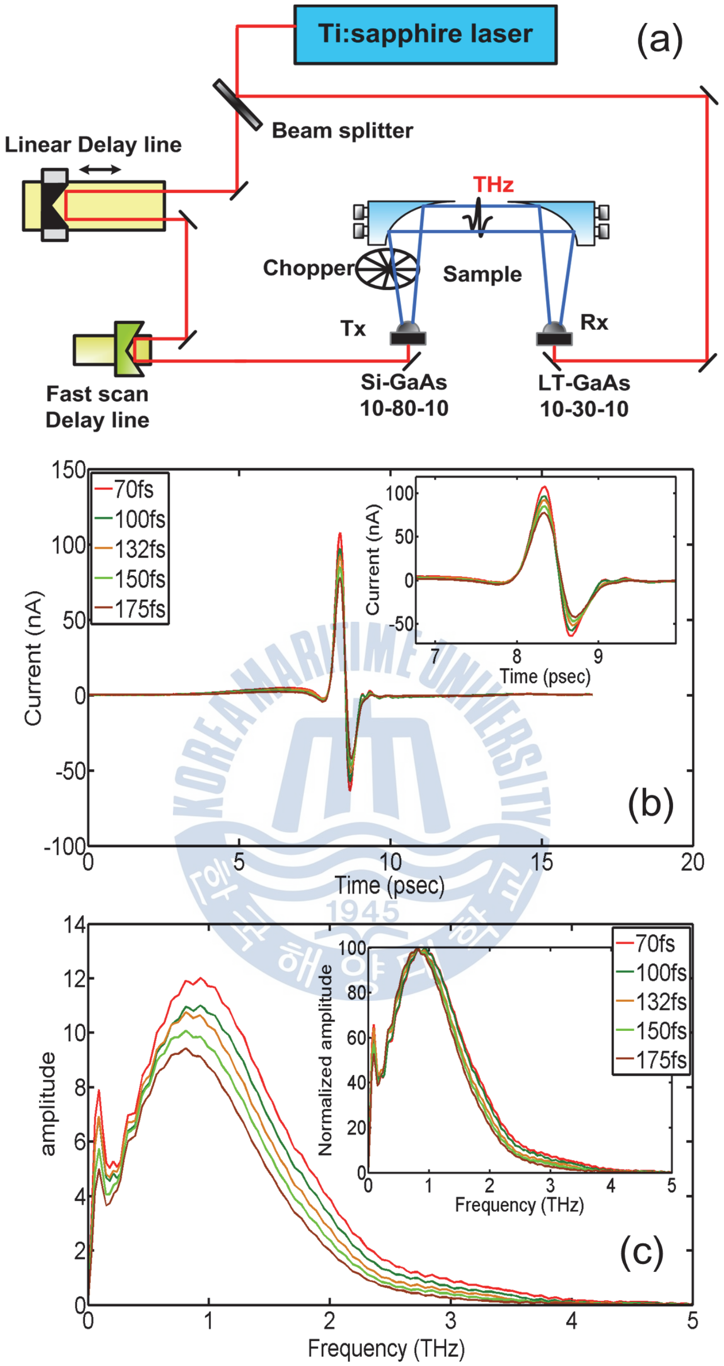

Figure 2-1 (a) Schematic diagram of the General THz-TDS system. (b) Measured THz signal dependent on the change of laser pulse width. (c) THz spectra of (b).

full width at half maximum (FWHM) of a laser pulse is defined as the pulse width. The measured amplitude and spectrum band width of THz waves vary depending on the laser pulse width [34]. The changes of THz waves depending on the laser pulse widths are depicted in figure 2-1. The altered THz time-domain signals and THz spectra are shown in figures 2-1 (b) and (c), respectively, as the laser pulse width changes from 70 fs to 175 fs.

As shown in figure 2-1, the peak-to-peak amplitude of the THz wave was reduced by 30%, from 171 nA to 119 nA, as the laser pulse width changed from 70 fs to 175 fs. The measured center frequency of the THz wave moved from 0.93 THz to 0.81 THz, and the band width was reduced from 1.39 THz to 1.25 THz for the FWHM value. The inset in figure 2-1 (b) is an enlargement of the time window with 7~10 ps, and the inset in figure 2-1 (c) shows the spectra normalized by the peak amplitude. It is demonstrated experimentally that the THz wave has a larger amplitude and broader band width as the laser pulse width becomes narrower.

When the femtosecond laser beam is passing through a material, positive group delay dispersion occurs (GDD). The GDD of a laser beam is the derivative of the group delay with respect to the angular frequency (ω), or the second derivative of the change in spectral phase:

$$GDD(\omega) = \frac{d^2\phi(\omega)}{d\omega^2} \qquad (1)$$

where $\phi(\omega)$ is the phase delay. A beam isolator and a half-wave plate are used in the fiber-coupled THz system to prevent reflection of the beam from any surfaces. Two 2-m-long optical fibers are also used in the system.

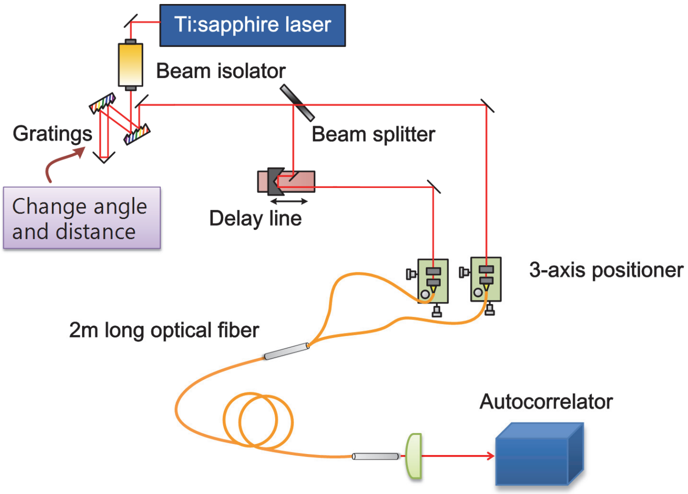

Figure 2-2 Schematic diagram of experimental setup for measurement of laser pulse width.

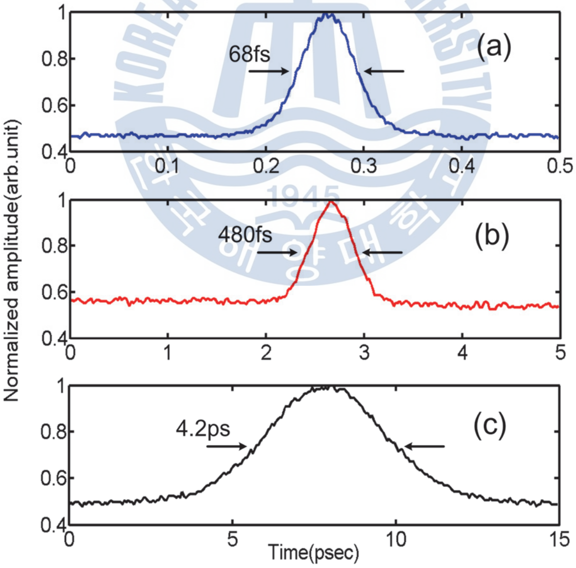

Figure 2-3 Measured full width at half maximum of laser pulse width (a) Laser pulse width without positive GDD (b) Dispersed laser pulse by the beam isolator (c) Dispersed laser pulse by the optical fiber which length is 2m.

These optical components consist of specific materials, and the positive GDD of the laser beam occurs as it passes through those materials. Serious positive GDD occurs when the laser beam passes through the beam isolator and optical fiber. An experimental setup for the measurement of laser dispersion is shown in figure 2-2, and the measured dispersion of the laser beam is shown in figure 2-3. The laser, with a pulse width of 68 fs, is dispersed approximately 7 times (480 fs) after passing through beam isolator, and 60 times (4.2 ps) after passing through the 2-m-long optical fiber. The negative GDD from the grating pair was able to compensate for the positive GDD.

2.1.4 Compensation of dispersed laser pulse

There are three methods to compensate a positively dispersed laser beam, using a chirped mirror, a prism pair, or a grating pair. The grating pair is frequently used to compensate large dispersed laser beams, such as laser pulses that have passed through long optical fibers.

The long-wavelength components of laser pulses pass quickly through a general material, and the short-wavelength components pass slowly through a material. As a result, positive GDD occurs, as shown in figure 2-4 (a). The incident laser pulses into the grating pair are diffracted at different angles depending on the wavelength, as shown in figure 2-4 (b). The diffraction angle θ_m is given by:

$$\sin\theta_m(\omega) = m\frac{\lambda(\omega)}{\Lambda} + \sin\theta_i \quad (m=0,\ \pm1,\ \pm2,\ ....) \qquad (2)$$

where λ is the wavelength, Λ is the grating period, and θ_i is the incident

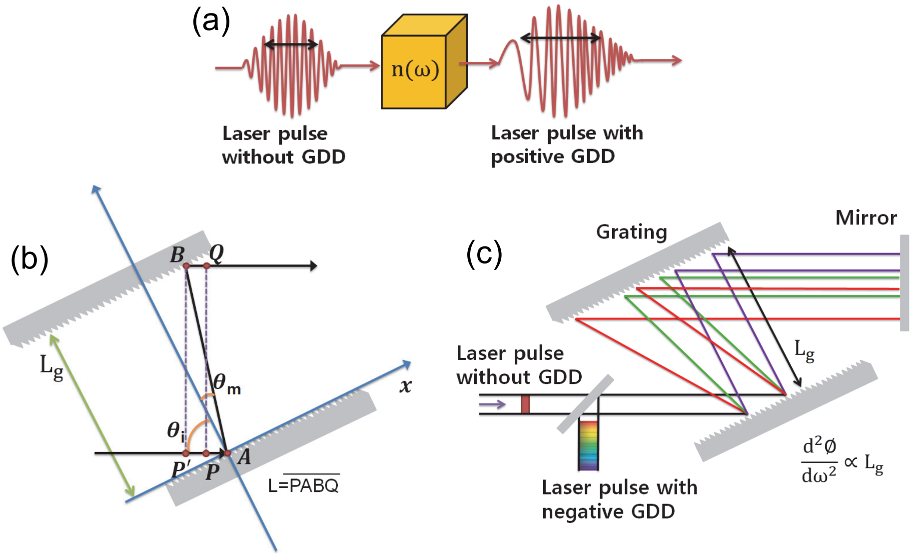

Figure 2-4 (a) Positive group delay dispersion (b) Geometry of incident angle and diffracted angle (c) Negative group delay dispersion by grating pair

angle. The geometrical path length L is given by:

$$L = \frac{L_g}{\cos\theta_m}[1+\cos(\theta_m+\theta_i)] \tag{3}$$

The diffracted long-wavelength components travel a larger distance than the short-wavelength components, and negative GDD thus occurs. The negative GDD of laser pulses are proportional to Lg, which is the distance between the grating pairs, as shown in figure 2-4 (c). In this study, the pulse compression is verified experimentally using an autocorrelator.

NT43-850 grating made by Edmond Optics company is used in this experiment for pulse compensation. There are 830 grooves per 1 mm of grating and the blaze angle is 19.23°. The negative GDD by the grating depends on the incident angle and distance between the grating pair so the negative GDD is investigated using a *Mini* autocorrelator made by APE at different angles and distances.

First, the changes of laser pulse depending on the distance between grating pair are investigated at fixed 50degree incident angle. When the distance is 70mm, the narrowest pulse width of 270fs was found. The measured time domain laser pulses by autocorrelator are depicted in figure 2-5 (a) and their pulse widths (FWHM) dependent on the distance between grating pair are shown in figure 2-5 (b).

The changes of the laser pulse depending on the incident angles into the grating pair are investigated at a fixed distance of 70 mm between the grating pair. The narrowest pulse width was found at 56 degrees (results not shown). Typically, a beam splitter is used in the pulse compensation experimental setup, as shown in figure 2-4 (c). But the output intensity of a laser pulse after passing through a beam splitter is just 25% the intensity of the incident laser pulse. As such, a retro reflector was used instead of a beam splitter to use all of the laser beam power in the pulse compensation

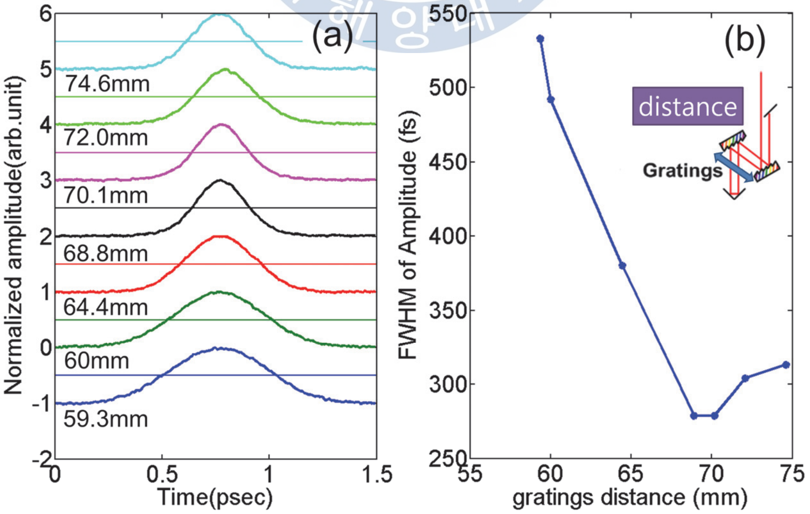

figure 2-5 (a) Measured laser pulse width dependent on the distance between two gratings (b) FWHM value versus distance of gratings setup, as shown in the inset in figure 2-5 (b).

The output intensity of a laser pulse after passing through the *NT48-850* grating pair was only 25% the intensity of the incident laser pulse. The 75% loss was caused by the grating pair, so the grating pair was replaced by a *715.704.160* grating pair made by the Spectrogon company. The output intensity of the laser pulse after the new grating pair was used was 48% of the incident laser beam intensity. The new optimized incident angle is 53 degrees, and the distance is 27 mm. The acquired pulse width was 182 fs.

2.2 Prototype THz endoscope (PTES) for modularization

2.2.1 Fabrication process of PTES

The final diameter of a TES must not exceed 10 mm for use in stomachs or colons. In order to fabricate the TES with diameter less than 10 mm, all parts must be miniaturized and modularized. As the parts of the TES become smaller, the fabrication process of the TES becomes difficult. Accordingly, the modularization of the TES was verified using a TES with a large diameter (>10 mm) before miniaturization. The large-diameter TES fabricated was referred to as the Prototype TES (PTES).

The fabrication process will be described as Tx of the PTES (the fabrication process of the Rx is same as that of Tx). Femtosecond laser pulses and a semiconductor chip with a photoconductive dipole antenna are needed to generate THz waves. An optical lens part consisting of a lens, lens mount, and optical fiber is needed to guide and focus the laser pulses on the antenna. Finally, a high-resistivity Si lens is needed to efficiently

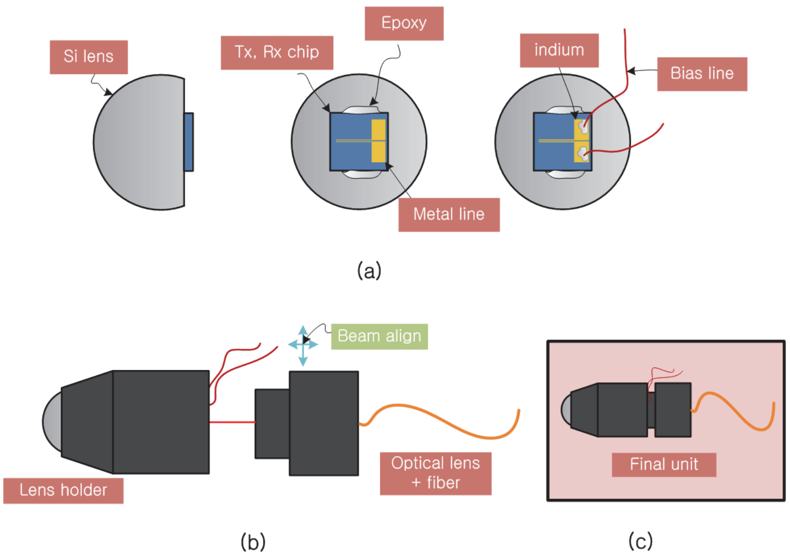

Figure 2-6 The process of manufacturing PTES. The diameter of PTES is 20mm and the length is 90mm.

radiate and collimate the generated THz waves to free space. The modularization process is shown in figure 2-6. The Tx semiconductor chip is positioned on the hemispherical Si lens, which has a diameter of 10 mm and height of 6.5 mm. The chip is fixed by epoxy adhesive as shown in figure 2-6 (a). The Tx antenna used consists of two 10-µm-wide metal lines separated by 200 µm, fabricated on semi-insulating (SI) GaAs. The Tx chip size is 6 mm X 6 mm. Two metal lines for the bias voltage are connected to a metal pad of the Tx chip using bulk indium, and are fixed using epoxy adhesive. The Si lens combined with the Tx chip dock with a custom-made lens holder with 18.6-mm diameter and 20.7-mm length, as shown in figure 2-6 (b). An *mp220* lens made by Thorlabs is combined with a 2-m-long optical fiber in another custom-made lens holder with 15.6-mm diameter and 20-mm length. The alignment of the laser pulse to the photoconductive antenna is very important to generate and detect the THz waves, and accordingly, the optical lens part is micro-aligned by an XY-translator with a micrometer. After the beam is completely aligned, the

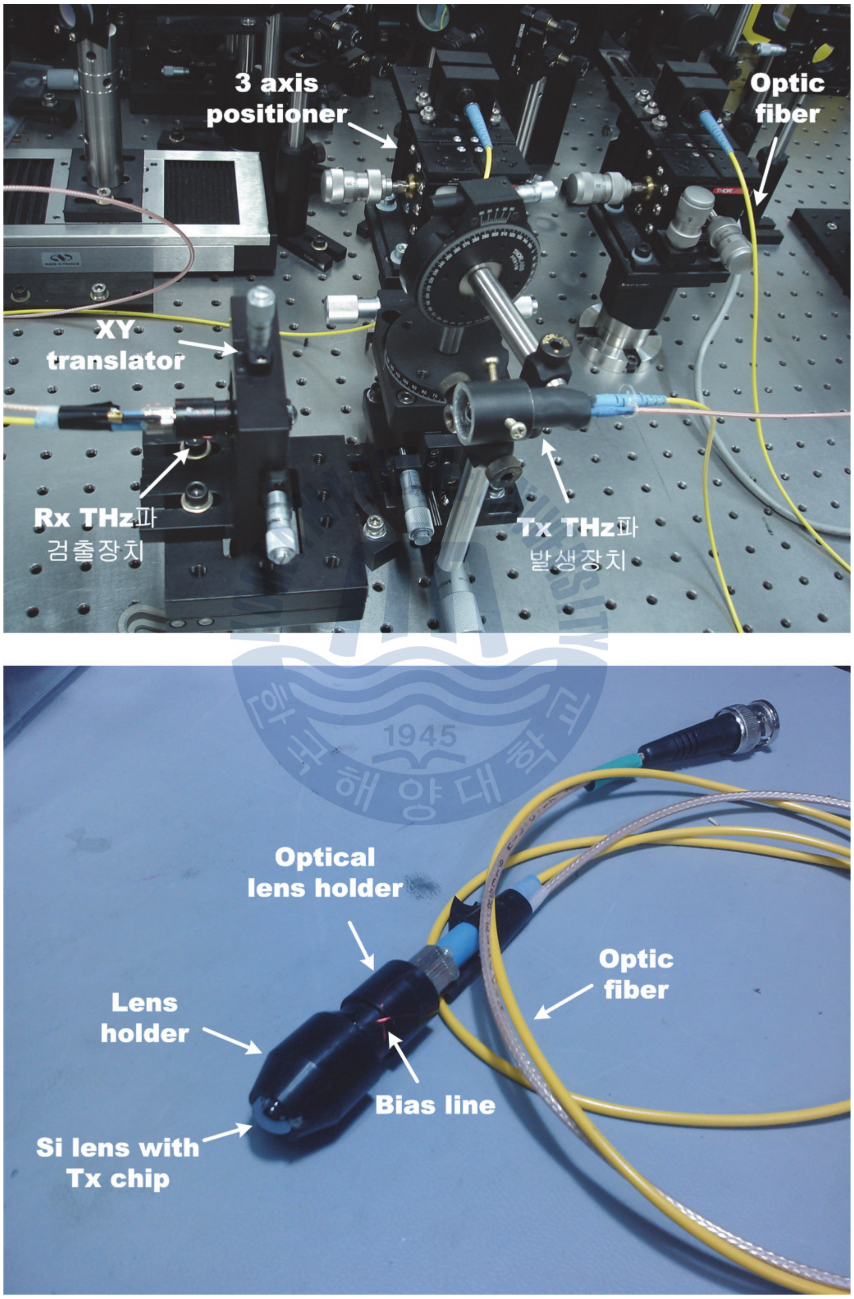

Figure 2-7 Photograph of manufactured PTES.

two lens holders are united by epoxy adhesive and removed again using the XY-translator. In figure 2-6 (c), the completely fabricated PTES is depicted. The Rx module of the PTES with a 10-30-10 dipole antenna structure (line width, distance between lines, line width, in μm) was fabricated using the same processes. A picture of the completed PTES is shown in figure 2-7. The final PTES is a device whose length is 90 mm and diameter is 20 mm. It can be used to measure THz waves moving freely.

2.2.2 Measured THz pulse by PTES

The whole THz experimental setup, including the fabricated PTES, is shown in figure 2-8. Negative GDD occurs to compensate for the positive GDD after the laser pulses with 68-fs pulse width have passed through the beam isolator and half-wave plate and travel through the grating pair.

Then, the dispersed laser pulses are split into Tx and Rx laser pulses by a beam splitter. The propagated laser pulses in free space are efficiently

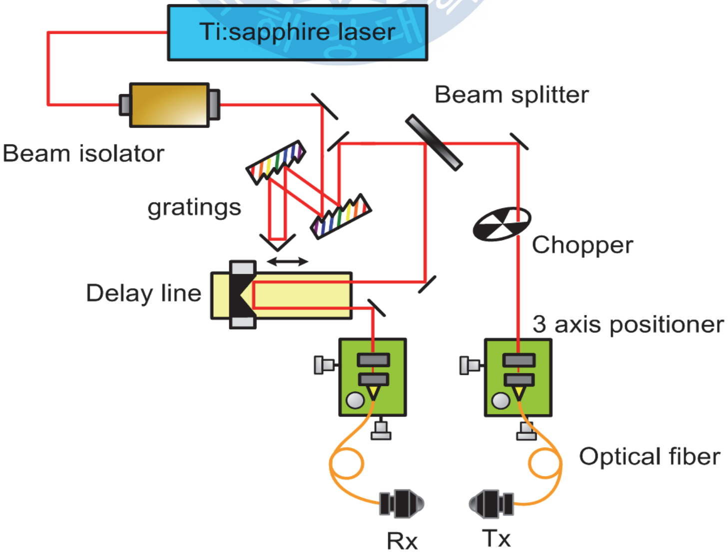

Figure 2-8 Experimental setup for PTES.

coupled with 2-m-long optical fibers by 3-axis-positioners with a proper optical lens. A motorized stage for time delay is inserted into the beam path of the Tx side. As the laser pulses compensated after passing through the 2-m-long optical fiber arrive at the Tx transmission line, holes and electrons are generated, and the generated carriers are immediately accelerated by the applied electric field. The THz waves generated by transient photocurrent radiate to free space by a high-resistivity Si lens, and are detected by an Rx chip on the opposite side.

Figure 2-9 (a) shows the THz pulse when the Tx and Rx modules are separated by 6 cm for face-to-face measurement. The peak amplitude of the measured THz signal is 1171 pA, and the FWHM of the THz pulse is 0.98 psec. The calculated signal-to-noise ratio (SNR) of the measured THz pulse is 950:1. As shown in Figure 2-9 (b), the corresponding amplitude spectrum obtained using a numerical Fourier transform extended beyond 1 THz. This result reveals that the fabricated PTES can measure high-qualitative THz waves moving freely.

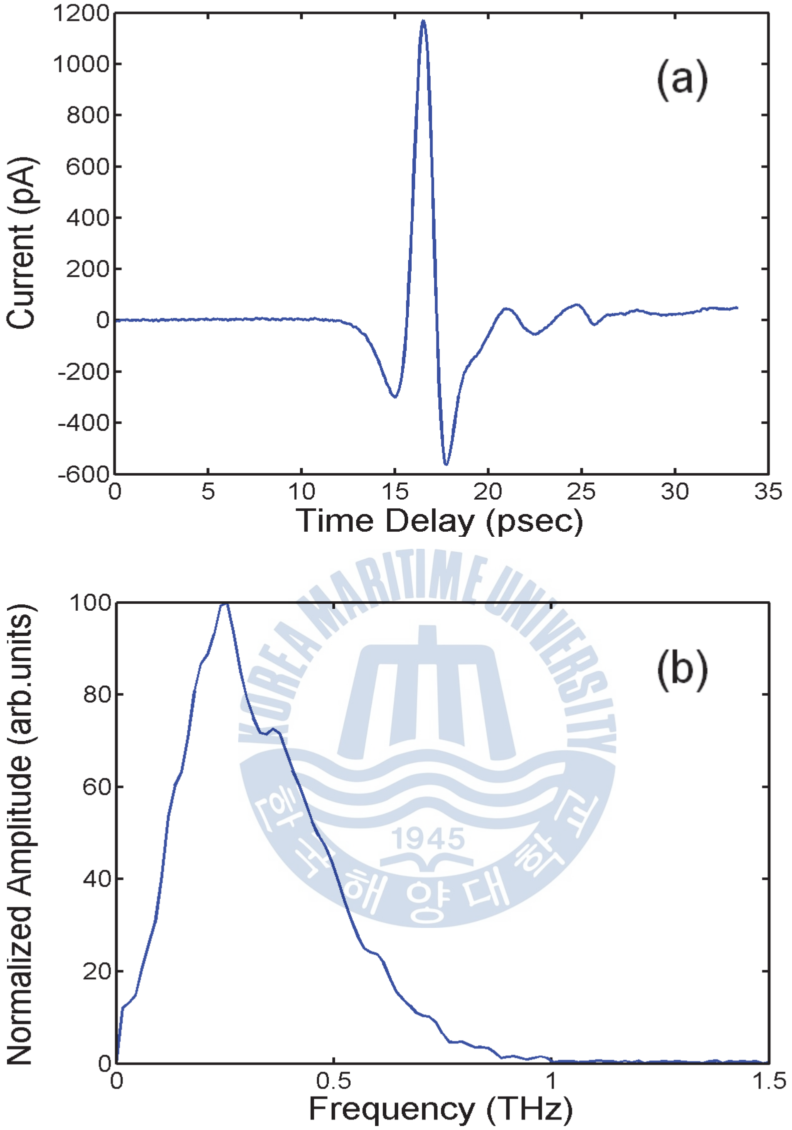

Figure 2-9 (a) Measured time domain THz signal by PTES (b) Spectrum of (a).

3. Miniaturized THz endoscope and its beam profile

3.1 Miniaturized THz endoscope (MTES)

The modularization of all parts of the TES was demonstrated by manufacturing the PTES in Chapter 2. In this Chapter, for practical applications, a TES with diameter less than 10 mm is fabricated by miniaturizing all parts of the PTES. *In-vivo* human body samples are measured by the miniaturized TES. This device is referred to as the MTES.

3.1.1 Preparation of miniaturized part of MTES

- Tx, Rx semiconductor chip: The Tx chip consists of a 10-200-10 photoconductive transmission line on SI-GaAS substrate, whose size is 1.8 mm X 1.9 mm with a thickness of 450 µm. The Rx chip consists of a 10-30-10 photoconductive dipole antenna and 5-µm gap, on an LTG-GaAs substrate whose size is 2 mm X 2.8 mm with a thickness of 350 µm. In figure 3-1 (a), a photograph of the Tx chip on an Si lens is shown.

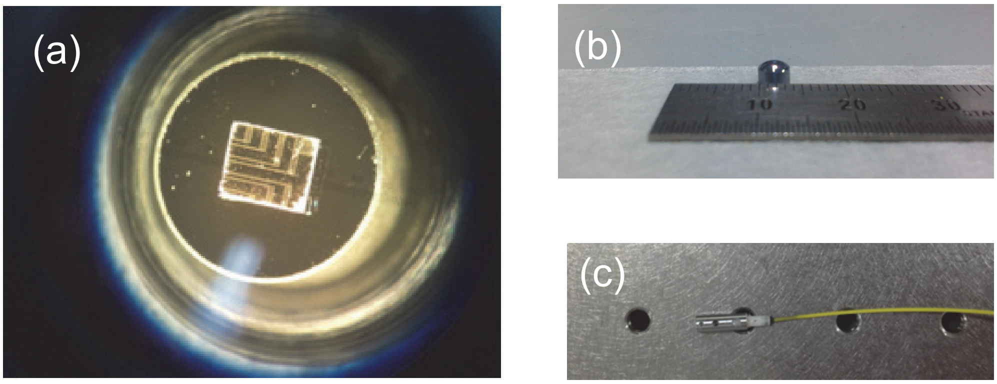

Fgure 3-1 (a) Tx SI-GaAs chip on a Si lens (b) Si lens with 4mm diameter (c) Combination of drum lens, convex lens and optical fiber

- Optical lens part with fiber: The optical lens part consists of a convex lens with 3-mm diameter and 1.5-mm thickness, a drum lens with 2.4-mm diameter and 3-mm thickness, a custom-made lens mount, and a 2-m-long optical fiber made by Thorlabs. A photograph of the assembled optical lens part is shown in figure 3-1 (c).

- Si lens: After the radius of curvature of the Si lens is determined, the radiated THz beam shape is determined by the height of the Si lens, and whether the THz beam will be spread out, or be collimated or focused [35]. The design of the Si lens is a very important component for THz wave radiation. The Si lens was designed using Zemax, which is lens design software based on ray-tracing. The Si lens for Tx used on the MTES is designed to collimate the generated THz waves, and the designed radius curvature is 2.5 mm, the diameter is 4 mm, and the height is 3.03 mm. The Si lens for Rx used on the MTES is designed to focus propagated THz waves into the Rx dipole antenna, and the designed radius curvature is 2.5

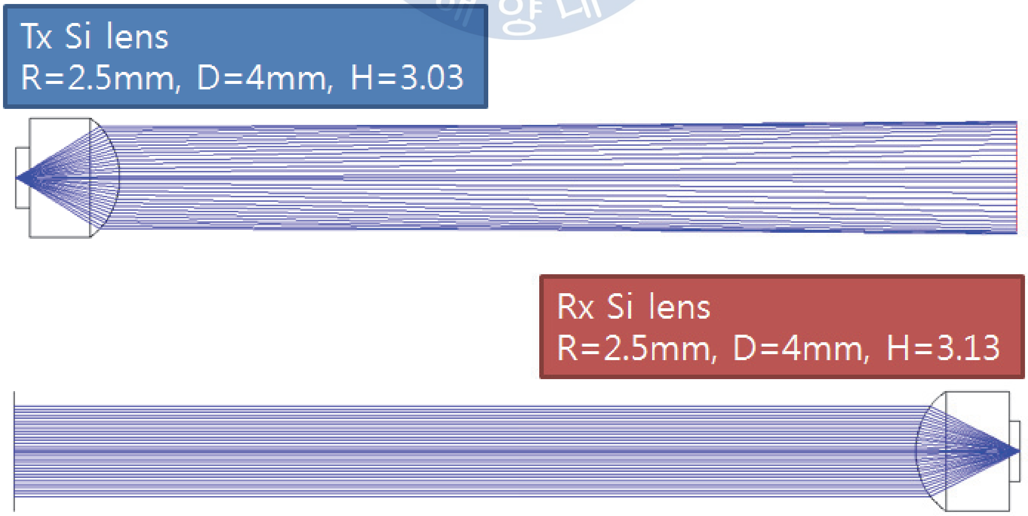

Figure 3-2 Simulated results by zemax program at 0.5THz.

mm, the diameter is 4 mm, and the height is 3.16 mm. Different heights of Si lenses result from different thicknesses of the Tx and Rx chips. The simulation results of THz radiation based on ray-tracing are shown in figure 3-2. The refractive index of the Si lens in the THz frequency regime is constant at 3.417. But the refractive indices of GaAs depend on frequency, so the shapes of THz radiation are altered by GaAs. However, because the difference in refractive indices at each frequency is small, the shapes of THz radiation are similar. The simulation result is depicted at 0.5-THz frequency in figure 3-2.

3.1.2 Fabrication process of MTES

The fabrication process is almost the same as that of the PTES, except for several minor problems caused by miniaturization. A 1.8-mm X 1.9-mm Tx chip is centered on a hemispherical Si lens with 4-mm diameter and 3.03-mm height, and fixed by epoxy adhesive. Two metal lines for bias voltage are connected to a metal pad of the Tx chip using bulk indium, and fixed by epoxy adhesive. The miniaturized Si lens is combined with a Tx chip dock with a custom-made 4-mm X 6-mm lens holder. The optical lens part is positioned at a proper distance from the focal point, and then all parts are assembled by epoxy adhesive. A schematic figure of the assembled miniaturized MTES is shown in figure 3-3. The final size of the fabricated Tx and Rx modules of the MTES is 4 mm X 6 mm X 27 mm. When the Tx and Rx modules are attached in parallel, their cross section is only (2 × 4 mm) × 6 mm (the diameter is less than 10 mm).

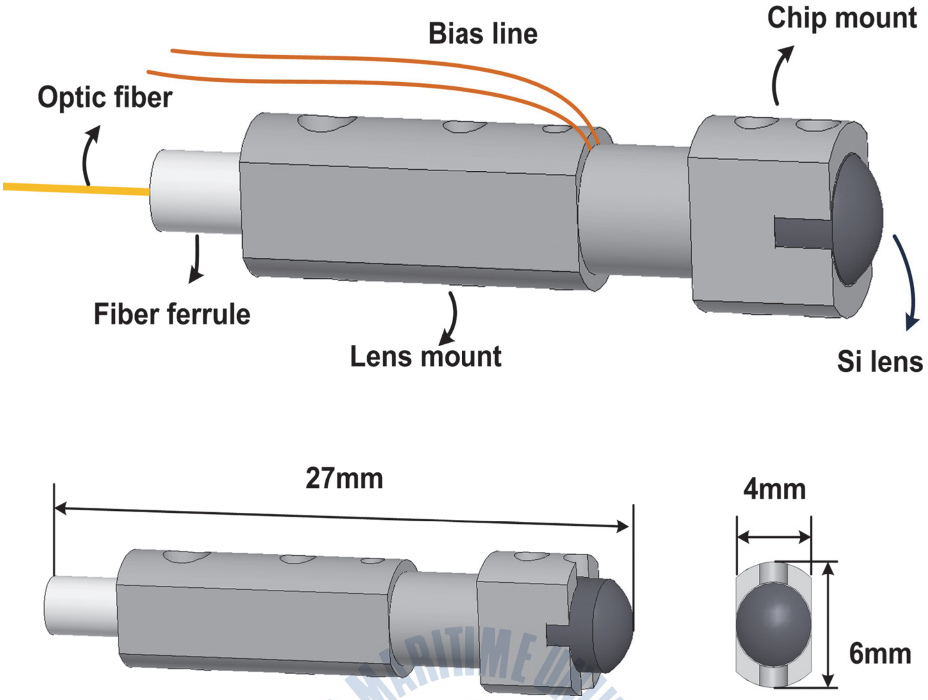

Figure 3-3 Schematic design of manufactured MTES which is miniatured compared with PTES. The whole dimension is 8mm X 6mm X 27mm.

The manufactured MTES can move freely in contrast to the fixed conventional THz-TDS, and the MTES is miniaturized compared with the PTES or fiber-coupled THz module made by Crooker. Thus, the MTES can measure *in-vivo* bio-samples of the human body, which cannot be measured by THz waves. To demonstrate the feasibility of measurement with the human body *in vivo*, the side wall of the mouth and the tongue, which cannot be measured by THz waves, are measured by the fabricated MTES. The whole schematic of the experimental setup for measurement of the human body *in vivo* is depicted in figure 3-4 (a), and photographs of the fabricated Tx module of the MTES are shown in figures 3-4 (b) and (c) [36]. The results of *in-vivo* measurement will be described later.

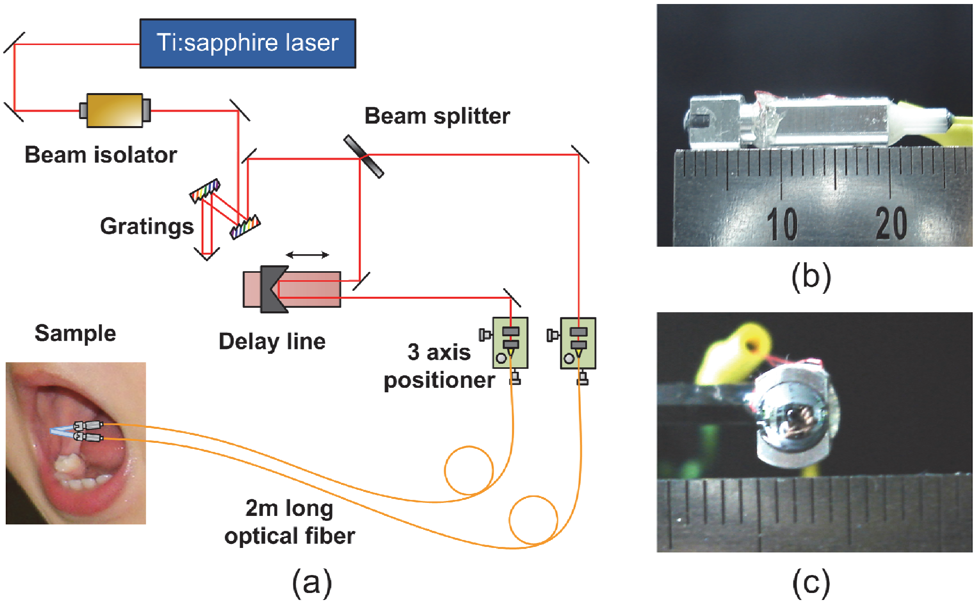

Figure 3-4 (a) Experimental setup for measurement of bio sample with *in-vivo* state. (b) Side view of Tx module. (c) Front view of Tx module [36].

3.2 Measured THz signal by MTES and its beam profile

3.2.1 Measured THz signal by MTES

Figure 3-5 shows the time-domain THz signal and its spectra measured by MTES when the Tx and Rx module are separated by 2 cm for face-to-face measurement. The THz pulse is obtained by a single measurement without any filtering process. The alignment between a semiconductor chip and an Si lens is carried out by verifying the measured THz signal, because the alignment greatly affects the THz measurement. However, the alignment was not carried out by verifying the measured THz signal in the fabrication process of the MTES. Because the alignment was accomplished using an optical microscope, there is a little bit of misalignment. Accordingly, there is a bump near 14 psec, since the THz antennas may not have been perfectly

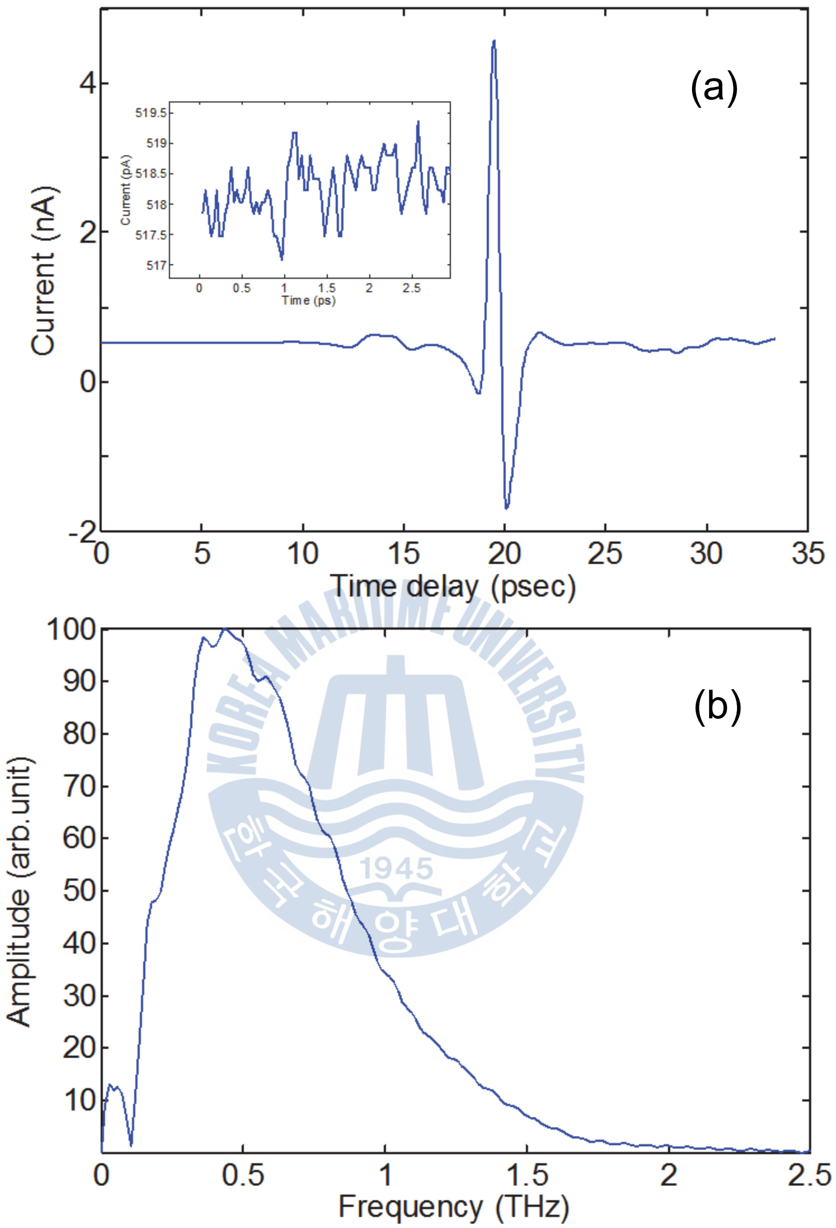

Figure 3-5 (a) Measured THz time domain signal by MTES (b) Spectra of (a).

positioned at the center of the Si lens, as shown in figure 3-5 (a). However, the amplitude of the bump is only 3.2% compared to the main THz pulse, which has a 6.2-nA peak-to-peak amplitude. Since the Tx and Rx modules of the MTES are located close together, the offset of the THz pulse assumed by the bias voltage is 520 pA. The inset graph in figure 3-5 (a) shows the noise signals measured over 0~2.5 ps. The calculated RMS value of the noise signal is 0.48 pA, while the peak-to-peak amplitude is 6.2 nA. The resultant SNR is 12000:1, which is extremely high. Although all parts related to THz generation and detection were miniaturized and optical fibers were used, the measured THz signal has very good quality. As shown in figure 3-5 (b), the corresponding amplitude spectrum obtained using a numerical Fourier transform extended to beyond 2 THz. The peak of the amplitude spectrum is 0.43 THz.

3.2.2 Beam profile of measured THz signal by MTES

The Rx module is moved by ±20 degrees from the center line, maintaining

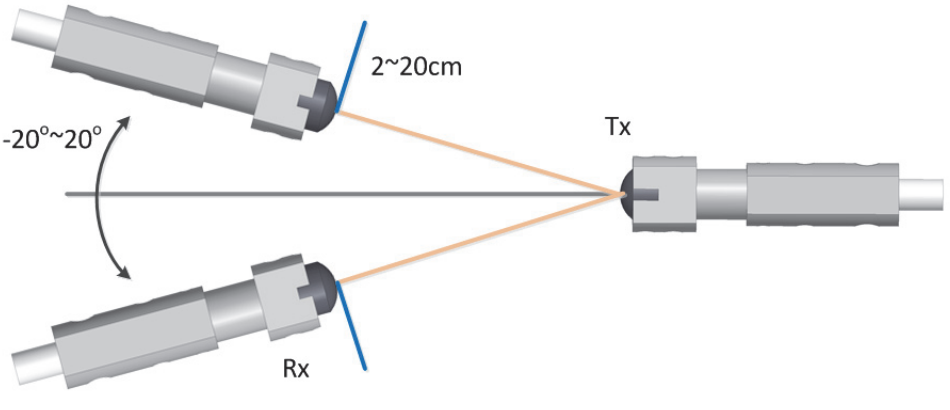

Figure 3-6 Schematic diagram of experimental setup for investigation of divergence of THz wave

2-cm separation, in order to determine any divergence in the THz radiation. The schematic figure is shown in figure 3-6, and the measured 3-dimensional time-domain THz pulses are shown in figure 3-7 (a) [36]. The

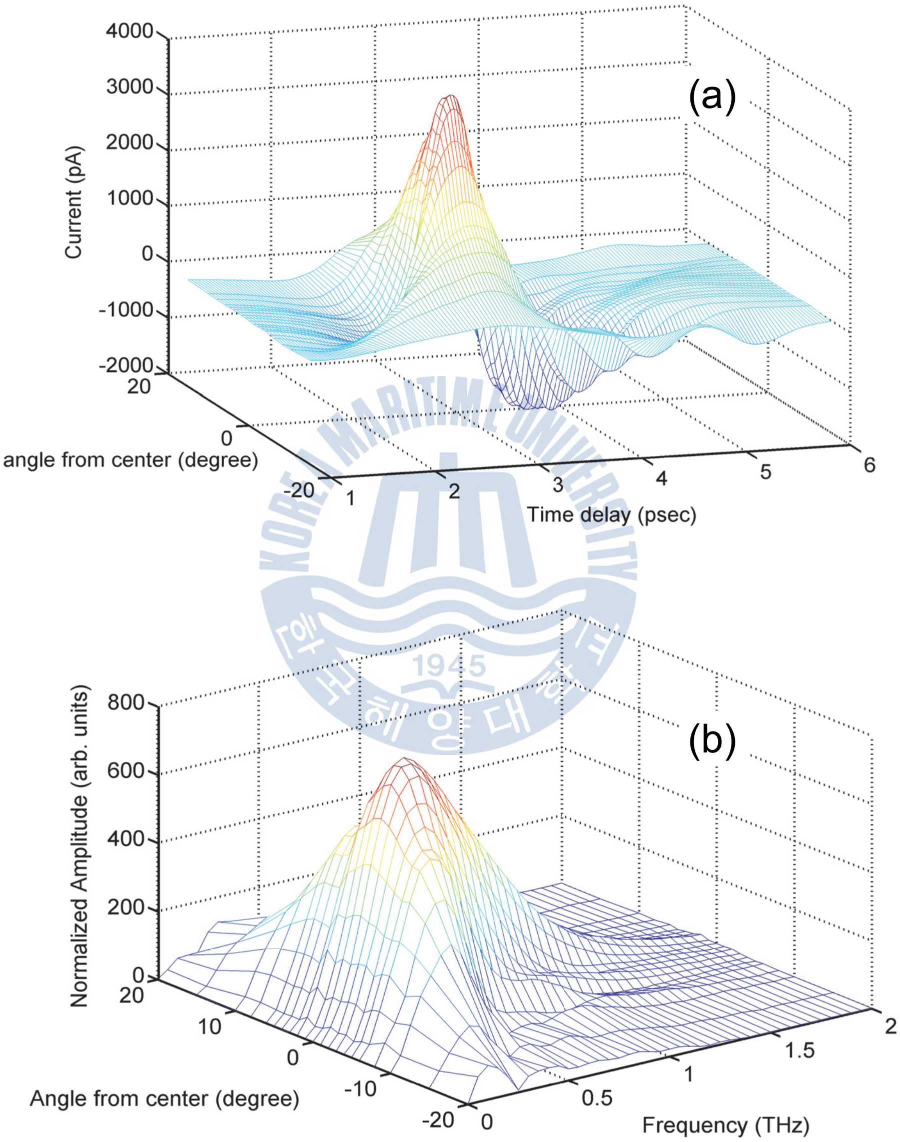

Figure 3-7 THz transmission measurement with different angles for 2cm separation between generator and detector modules (a) Time domain THz pulses. (b) Spectra [36].

amplitude is dramatically reduced upon increasing the angle, which depends on the 3-dimensional THz spectra of each pulse, as shown in figure 3-7 (b). The spectrum amplitude and bandwidth are also dramatically reduced upon increasing the angle. Because of the Si lens design, most of the THz energy concentrates at the center. Figure 3-8 shows the peak-to-peak pulse amplitude with different distances between the generator and detector [36]. The dots represent the experimental data and the solid curves represent the Lorentzian fits. When the measurement is normalized, the exp(−1) exists at ± 8.1 degrees at 2 cm separation. When the Rx module is moved back, the distance between the Tx and Rx modules is increased from 8 cm to 12 cm, 20cm and the peak-to-peak pulse amplitudes are reduced to 2 nA, 1.3 nA, and 0.7 nA, respectively. In order to obtain larger THz signals, the incident angle and distance to the target should be small.

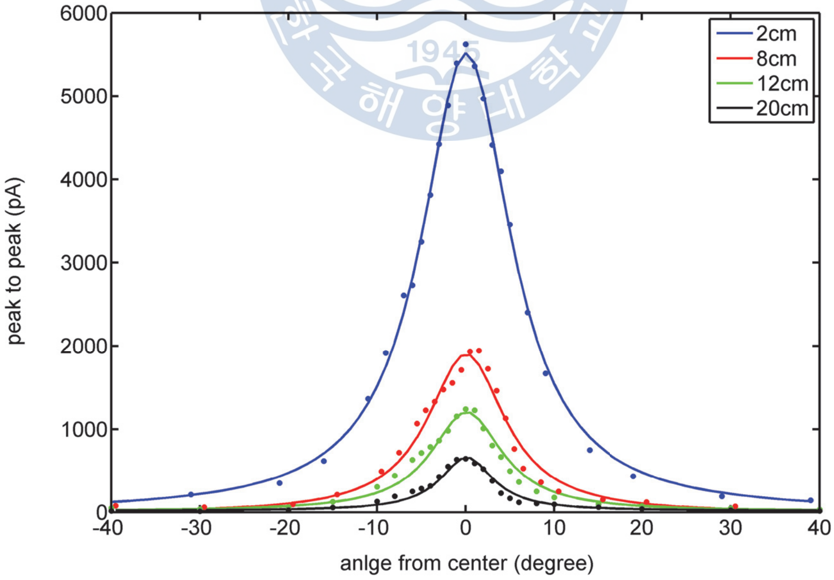

Figure 3-8 Angle dependent peak-to-peak THz amplitude with different separations [36].

3.3 Application of MTES for *In-vivo* experiment

3.3.1 Mount coupled MTES for reflection measurement

Since the fiber coupled Tx and Rx modules of MTES are fixed robustly by epoxy adhesive, the beam alignment does not break under any circumstance. The transmission method has been used for analysis in typical THz-TDS systems. However, in order to analyze highly conductive materials such as doped semiconductors or highly absorptive materials such as water, the reflection method is often used in THz-TDS systems [37]. About 70% of the human body consists of water, so the reflection method should be used for the TES. In other to obtain identical reflected THz waves, a new measurement system was designed and fabricated as shown in figure 3-9. The Tx and Rx modules are fixed at an angle of 20 degree on a custom-made mount, and the reflection distance between Si lenses and

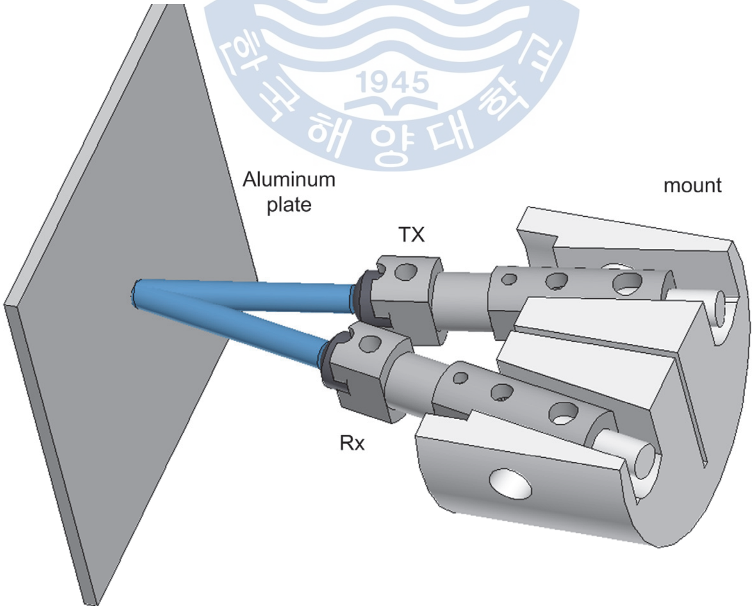

Figure 3-9 Mount coupled MTES for reflection measurement.

sample is always 1.5 cm. For practical applications, including THz measurement from the stomach and colon, The Tx and Rx modules should be combined in parallel with diameter under 10 mm. However, many

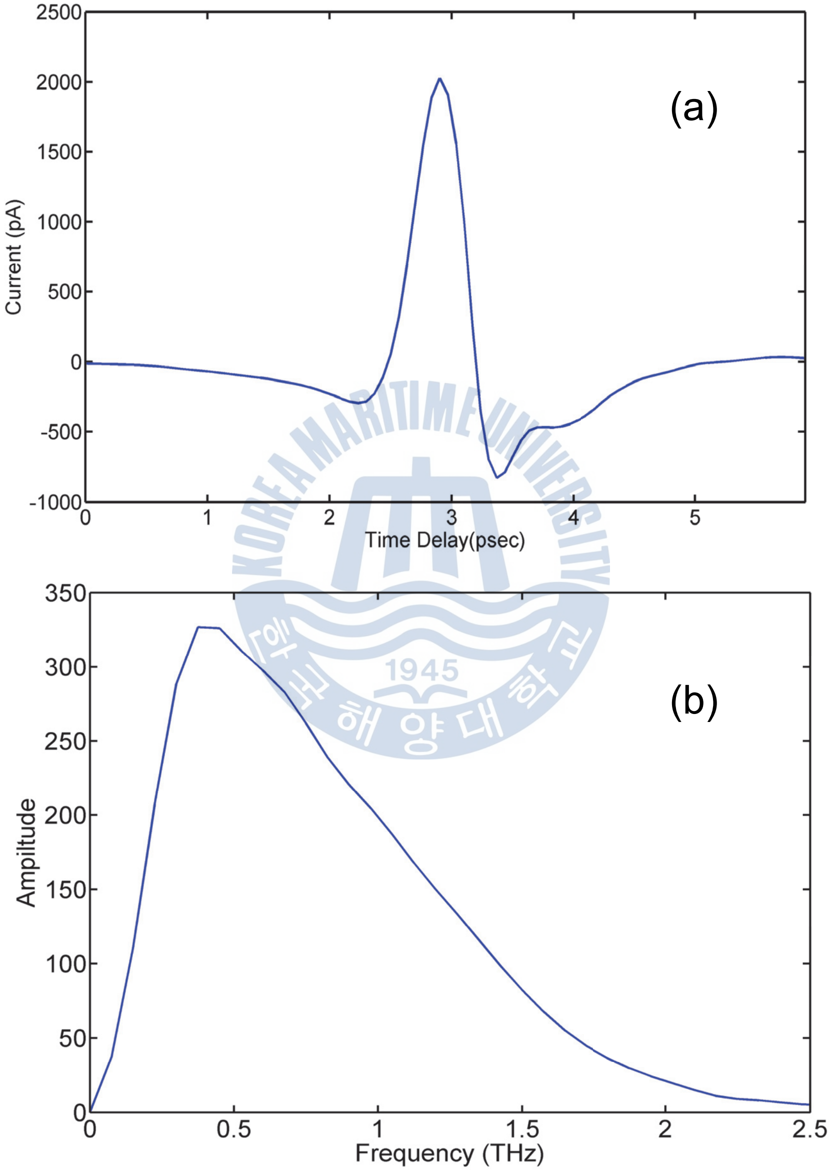

Figure 3-10 (a) Measured time domain THz signal by mount coupled MTES (b) Spectrum of (a).

procedures have remained for clinical demonstration, and confirmation is needed of whether the fabricated MTES can distinguish *in-vivo* samples of human body. The new measurement system was manufactured to address this. Since a metallic surface is an almost perfect conductor in the THz frequency range [38], the Tx and Rx modules are coupled properly with a custom-made mount, to verify the totally reflected THz pulses from an aluminum (Al) plate. The reflected THz pulse passing through a 3-mm-thick Teflon plate is depicted in figure 3-10. The measured peak-to-peak amplitude is 2.8 nA, and the THz spectrum extends up to 2.3 THz. There are sufficient THz amplitude and spectra for analysis of the experimental results.

3.3.2 Use of teflon plate cap for flat surface of samples

The reflected THz signal measured using the MTES from the palm of a hand was very small in reflection measurements. Because the palm of a hand is not flat like metal plates, the reflected THz pulse travels to a different direction whenever the THz wave is reflected from the palm of a hand. In order to overcome this problem, a Teflon plate was used, as shown in figure 3-11. The refractive index of Teflon is almost constant at 1.44 in the THz regime, and the absorption of Teflon is very low under 2-THz frequency [39]. The Teflon plate provides a flat surface under any surface of the samples. The reflected THz signal with the Teflon plate from the palm of a hand is larger than without a Teflon plate. The same results were obtained in repeated experiment using the Teflon plate. In order to create the same experimental conditions, a 3-mm thick and 15-mm-diameter Teflon

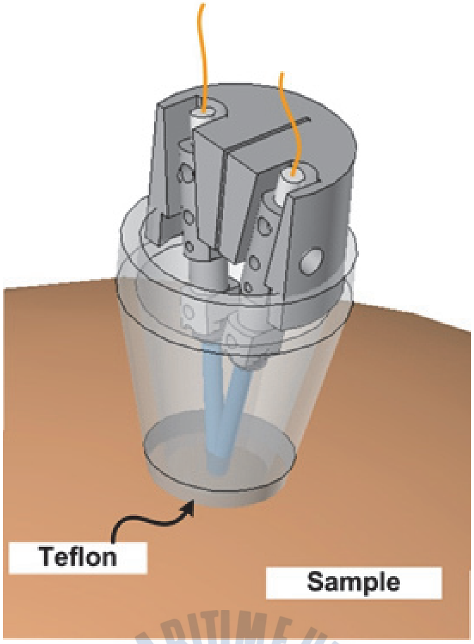

Figure 3-11 Teflon plate cap for making flat surface of samples.

plate was attached to the modules in the shape of a cap, as shown in figure 3-11.

3.3.3 Measuring bio samples with *in-vivo* state.

Figure 3-12 (a) shows the measured reflective THz signals from the side wall of the mouth, tongue, palm skin, water, and Al surfaces [36]. The pulses are numerically shifted for comparison. After the measurement of the THz reflection from the Al surface, the Al surface is replaced by the samples. Since the metallic surface is an almost perfect conductor in the THz frequency range, as mentioned earlier, the reflected THz pulse from the Al surface is considered as a reference. Because of the refractive index of water in the THz frequency range [40-41], the peak-to-peak amplitude of the

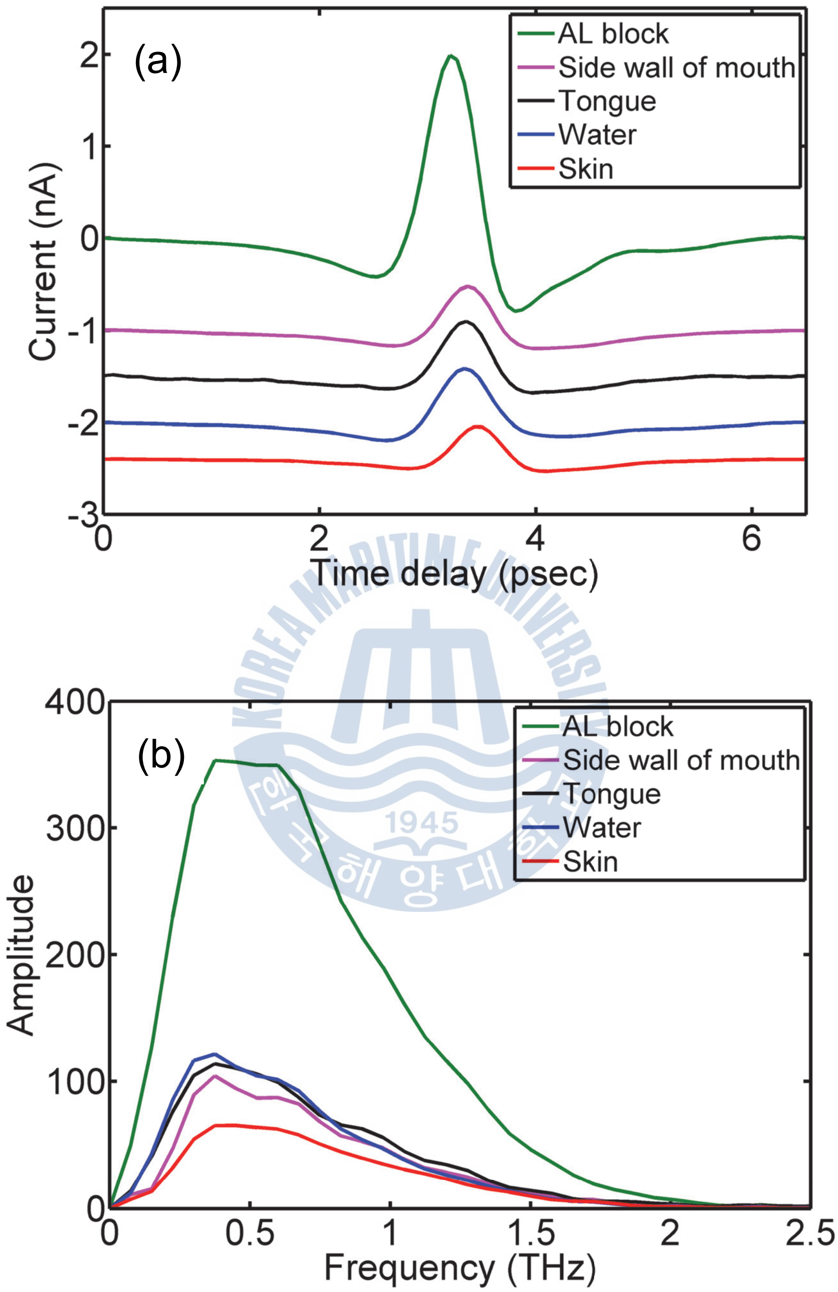

Figure 3-12 (a) Measured THz pulses by reflection measurement. (b) The respective spectra [36.]

reflected THz pulse is reduced by approximately 73% compared with the reference. As the human body is composed mostly of water (70%), the THz pulses reflected from the side wall of the mouth and tongue are also reduced by 76% and 73%, respectively. However, the THz pulse reflected by the skin is reduced by about 83%, which is 10% smaller than the amplitude of the water reflection, primarily because the dryness of the skin results in a refractive index that is a bit lower than that of water [40,41]. Figure 3-12 (b) shows the spectra of the samples. The reference spectrum extends up to 2.5 THz, while the relative amplitude of the other samples extends to 2.0 THz, because of less reflection at high frequencies. The amplitude of the side wall of the mouth, tongue, and water are somewhat different, whereas that of the skin is much lower at the measured frequency range. The ratio of the skin at 0.5 THz are only 73% and 62% compared to those of the side wall of the mouth and tongue, respectively.

3.3.4 Analysis of bio sample measurements

Since the reflected THz signals have magnitude and phase information for the samples, the refractive index and power absorption will be measured without Kramers–Kronig (K-K) analysis [37]. The incident THz pulse is radiated at 10 degrees into the Teflon plate, and the angle of the transmitted THz pulse is 7 degrees. The transmitted THz pulse becomes the incident THz pulse into the samples as shown in figure 3-13 (a). The incident angle and transmit angle of THz pulse at the boundary of samples affect the reflected amplitude of THz pulses from samples, and the value of concern

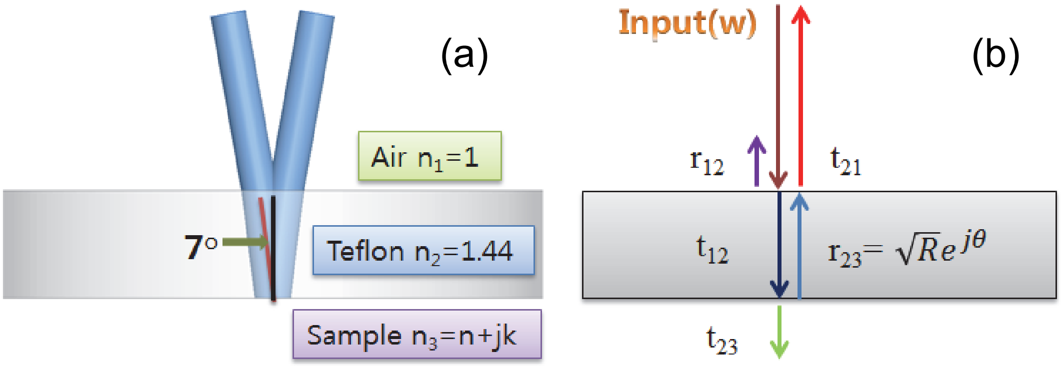

Figure 3-13 (a) Incident THz pulse into samples passing through a teflon plate (b) Reflections and transmissions of the incident THz pulse at 0 degree.

is in cosine form. The value of cos(7°) is 99.2% that of cos(0°). Accordingly, the angle of an incident THz pulse was considered 0 degrees for simplification of the analysis as shown in figure 3-13 (b).

The reflected THz pulse from the Al plate is:

$$Output_{AL}(w)=Input(\omega)\cdot t_{12}\cdot r_{23(AL)}\cdot t_{21}\quad (r_{23(AL)}=\ 1) \tag{1}$$

and the reflected THz pulse from a sample is:

$$Output_{S}(w)=input(\omega)\cdot t_{12}\cdot |r_{23(Sample)}|\cdot t_{21}\ =\ output_{AL}(\omega)\cdot |r_{23(Sample)}| \tag{2}$$

where t_{12} is the transmission coefficient from air to the Teflon plate and t_{21} is the transmission coefficient from Teflon plate to air. $r_{23(AL)}$ is the reflection coefficient from the Al plate and $|r_{23(Sample)}|$ is the magnitude of the reflection coefficient from the interface between the Teflon plate and a sample. Because of the very small power absorption by the Teflon plate, the absorption by the Teflon plate is neglected.

The reflection coefficient ($r_{23(Sample)}$) is given by:

$$r_{23(Sample)}=Re^{j\theta} \tag{3}$$

where R is the magnitude ratio, and θ is the phase of $r_{23(Sample)}$. These can be obtained by experimental results. These are given by:

$$|r_{23(Sample)}| = R(\omega) = output_S(\omega)/output_{AL}(\omega) \tag{4}$$

$$\theta(\omega) = \theta_S(\omega) - \theta_{AL}(\omega) \tag{5}$$

where θ_S and θ_{AL} are the phase of the reflected THz pulse from the sample and Al plate, respectively. $r_{23(Sample)}$ can also be expressed by:

$$r_{||23(Sample)} = \frac{n_3 - n_2}{n_3 + n_2} \tag{6}$$

where n_2 is the index of refraction of a Teflon plate and $n_3 = n + jk$, as shown in figure 3-13 (a). Substituting equation (eq.) (6) into eq. (3) and using Euler's formula, $e^{j\theta} = \cos\theta + j\sin\theta$,

$$\frac{(n - n_2) + jk}{(n + n_2) + jk} = R(\cos\theta + j\sin\theta) \tag{7}$$

After expanding eq. (7), and dividing the equation into a real part and imaginary part, eqs. (8) and (9) can be obtained as follows:

$$\text{Real term: } n - n_2 = nR\cos\theta + n_2R\cos\theta - kR\sin\theta \tag{8}$$

$$\text{Image term: } k = kR\cos\theta + nR\sin\theta - n_2R\sin\theta \tag{9}$$

eq (9) is simplified by k:

$$k = \frac{nR\sin\theta + n_2\sin\theta}{1 - R\cos\theta} \tag{10}$$

Substituting eq. (10) into eq. (3), the real index of refraction of n_3 can be obtained as

$$n = \left\{\frac{1 - R^2}{1 + R^2 - 2R\cos\theta}\right\} n_2 \tag{11}$$

In the same manner, the image index of refraction of n_3 can be obtained. In order to express this more intuitively, the notation n_2 is changed to n_{tef}, and n and k are rewritten as follows:

$$n = \left\{ \frac{1 - R^2}{1 + R^2 - 2R\cos\theta} \right\} n_{Tef} \tag{12}$$

$$k = \left\{ \frac{2R\sin\theta}{1 + R^2 - 2R\cos\theta} \right\} n_{Tef} \tag{13}$$

The relationship between the imaginary refractive index and power absorption is α=4πfk/c, where f is a given THz frequency and c is the speed of light. The measured refractive index and power absorption are shown in figures 3-14 and 3-15 [36]. The solid lines indicate fitting curves for the measurements. Because the refractive index of the Teflon is very sensitive to temperature, the phase information cannot be taken precisely. Therefore, it was measured it several times, and the ensuing error bars are marked in the figure. The refractive index and power absorption of water are very similar to previous measurements [40]. While the side wall of the mouth and tongue possess similar characteristics to those of water, the skin has a much lower refractive index and power absorption. Human adipose tissue (fat) has a much lower refractive index and power absorption compared to healthy skin [41]. Therefore, the skin changes in characteristics depending on its adipose contents.

In order to realize a THz endoscopic system, a millimeter-size generator and detector modules were developed ((2 × 4 mm) × 6 mm cross section), excited by an optical fiber-guided femtosecond laser. The peak-to-peak amplitude of the THz signal is 6.2 nA, and its spectrum extends up to 2 THz in face-to-face measurement. The modules were inserted into the mouth to simulate THz endoscopy, and the reflections were measured from the side wall of the mouth and tongue. From the measurements, the absorption and dispersion of the samples were obtained without K-K analysis. The refractive index and power absorption of the side wall of the mouth and tongue are similar to those of water. This might be due to the moist surfaces of the side wall of the mouth and tongue. To develop commercial endoscopes, this problem with moisture on internal organics has to be overcome by the suction of water or liquids from the surfaces. The values obtained for the skin are lower because of the skin’s adipose content. If the surfaces of soft internal organs changed, it can be expected that the THz beam can detect the surface conduction, which would show the possibility of using a THz endoscope to detect changes in tissues within the human body. With this miniature endoscopic system, THz signal detection for the respiratory tract and stomach will be performed in the future.

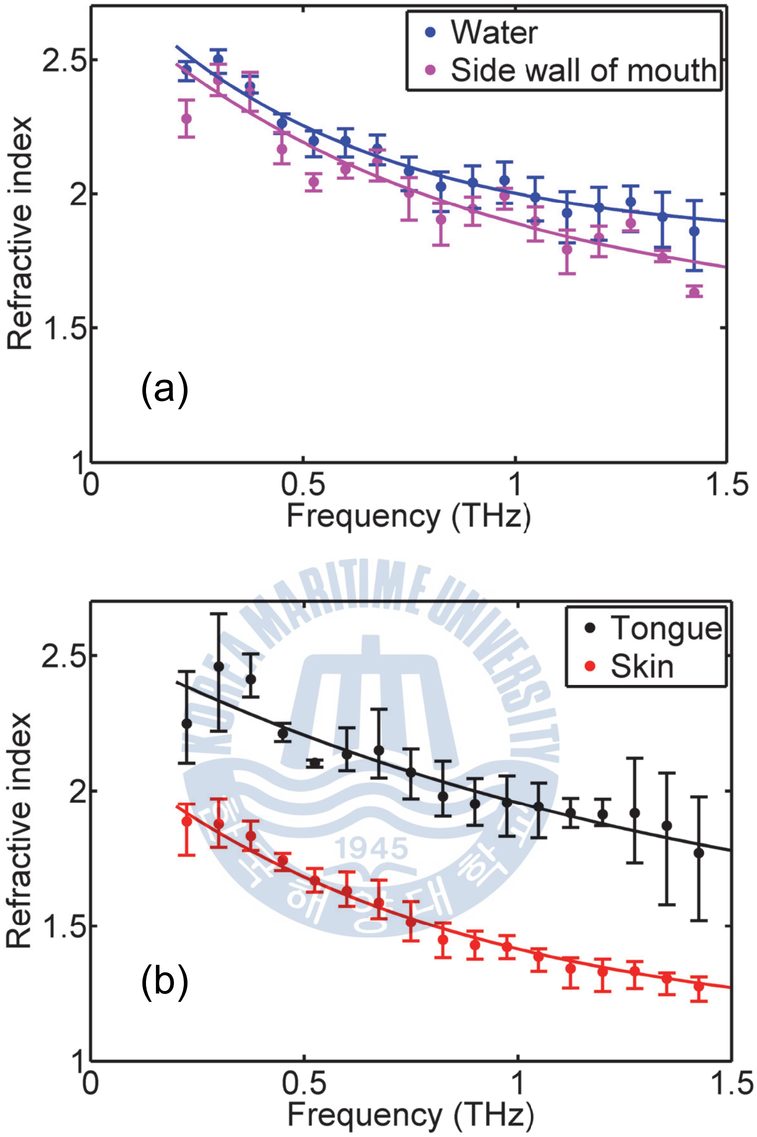

Figure 3-14 (a) Refractive index of water and side wall of mouth. (b) Refractive index of tongue and skin [36].

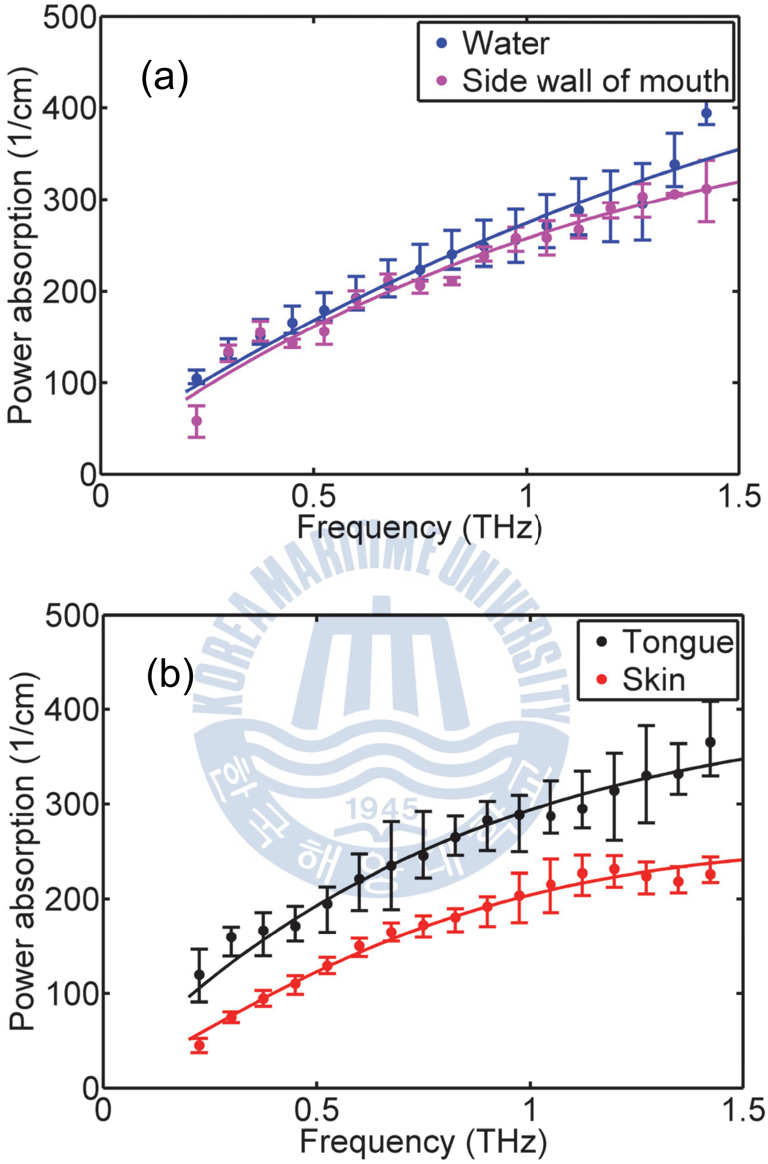

Figure 3-15 (a) Power absorption of water and side wall of mouth. (b) Power absorption of tongue and skin [36].

4. Super miniaturized THz endoscope

The miniaturized TES (MTES) was described in Chapter 3. It was mentioned that the MTES can be applied to stomach or colon measurements because of its small diameter, but it is difficult to apply the MTES to stomach and colon measurements on its own. It is difficult to make a THz image using the MTES alone, so it should be used with an optical endoscope in the present situation. In addition, as mentioned in Chapter 1, in order to distinguish between cancer and typical inflammation, a specific technique with GNRs named CATHI (contrast-agent-enabled THz imaging) is used for cancer diagnosis in some cases. The CATHI technique is needed using a CW infrared laser. Therefore the final diameter of the MTES combined with an optical endoscope and an infrared laser may exceed 10 mm in diameter. Accordingly, more advanced miniaturization of the TES is required for practical applications, so in this chapter, manufacturing methods for a super miniaturized TES (SMTES) are proposed.

4.1 Problems for miniaturizing

The fabricated MTES in Chapter 3 was separated by Tx and Rx modules, which limited the miniaturization of the separated type of TES. Therefore, to achieve super miniaturization, an integration method that involves uniting the separate Tx and Rx modules into a single module has been used. If this integrating method is directly applied to the MTES, the diameter is reduced to less than 5 mm or even smaller, although the size of all parts of the

MTES is the same. The device which can generate and detect electromagnetic waves as a single module is referred to as the transceiver.

4.2 Single-antenna THz transceiver (SATT)

4.2.1 Previous study of SATT

The single-antenna THz transceiver (SATT) was introduced primarily by Tani et al. in 2000 [42]. Optical pulses (Tx and Rx) generated by a Michaelson interferometer illuminate a single photoconductive antenna on LTG-GaAs with 9-V bias voltage and a lock-in amplifier. The first laser pulse generates a THz pulse, and the second pulse detects the propagated THz pulse with the same antenna. C. Jordens et al. reported about an SATT that obtained THz pulses with 100:1 SNR using a 3-dB optical fiber and an RC filter [27]. Because the THz pulse obtained by Jordens' method is better than that of Tani, and an optical fiber was used in Jordens' method, the method was first applied to the SMTES.

4.2.2 Measured THz signal by SATT and origin of noise

The SATT for the SMTES employed the same method reported by Jordens et al., and the THz pulse obtained by the SATT is depicted in figure 4-1. Although all conditions were the same as in the reference [27], the obtained SNR of the THz pulse is only 35:1, which is very low quality. Despite the large 1.2-nA peak-to-peak amplitude of the THz pulse, the acquired SNR is very low, because of the very high amount of noise in the signal. In order to establish the cause of the large noise signal, the fabricated SATT is used

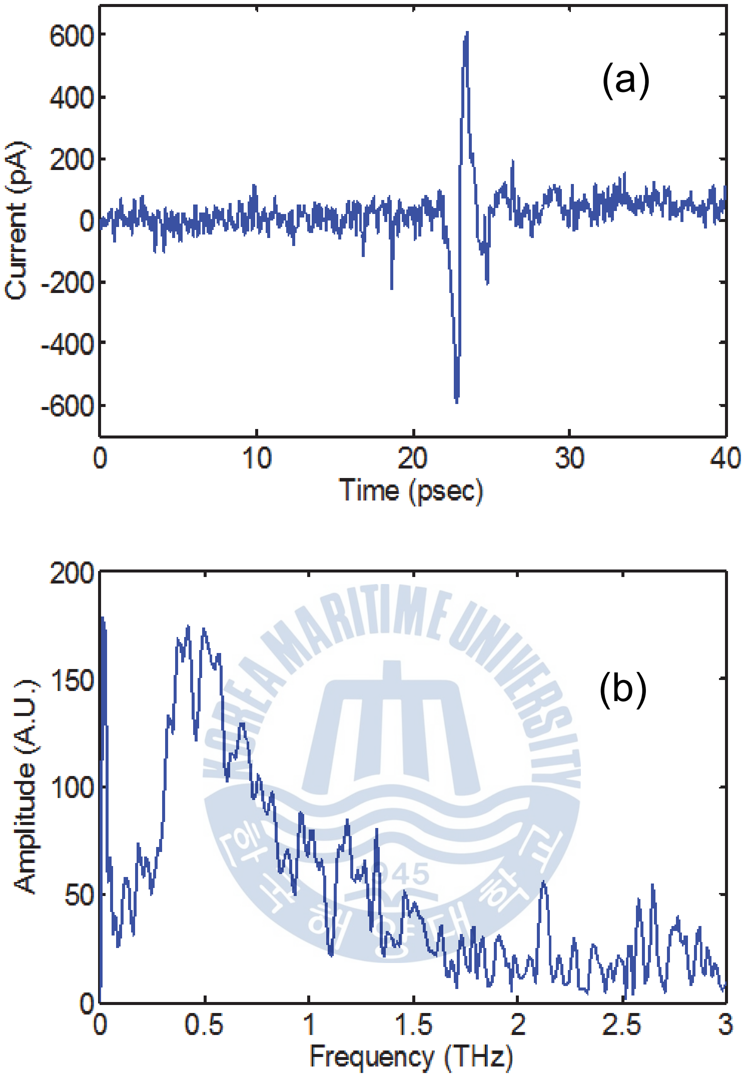

Figure 4-1 (a) Measured time domain THz signal by fiber-coupled SATT (b) Spectrum of (a).

only as an Rx to detect the propagated THz pulse generated by another fiber-coupled Tx. When the SATT is used as Rx, the measured THz pulses depending on the bias voltage to Rx are shown in figures 4-2 (a) and (b). The peak-to-peak current was Increased, and the noise signal was also

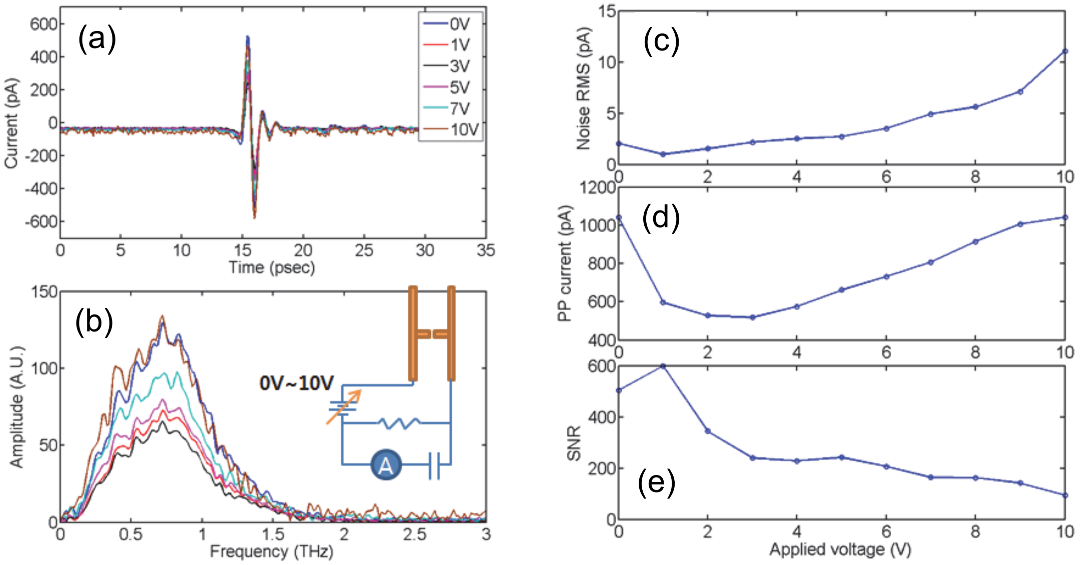

Figure 4-2 (a) Measured time domain THz signal by fiber-coupled SATT for only Rx (b) Spectrum of (a). (c) Measured RMS value of noise current (d) Peak to peak amplitude of THz signal (e) Calculated SNR of measured THz signal.

increased as the bias voltage increased. The resultant reduction of the SNR was verified experimentally, and the results are depicted in figure 5-2 (c), (d), and (e). I assume that a sharp decrease of the peak-to-peak amplitude in the range of 0V to 1V is caused by the changing input impedance as the bias voltage is applied to the dipole antenna. The fundamental cause of the reduced SNR is the DC bias voltage applied to the SATT.

For practical application of the TES to the human body, the chopper methods are limited to two. One involves an optical chopper located in the path of the Tx laser, and another uses AC bias voltage. However, when the two chopping methods are used experimentally with the SATT, the noise signal is too huge to be applied to the SATT. Accordingly, the SATT cannot be applied to the SMTES. So, another method which involves using twin photoconductive antennas on one chip is applied to SMTES to reduce the noise signal from the DC bias voltage.

4.3 SMTES using twin antenna THz transceiver (TATT)

As mentioned, the main cause of the noise signal is the DC bias voltage to generate THz pulses. To overcome this problem, a twin-antenna THz transceiver (TATT) was used for the SMTES. In 2002, Tani and Sakai knew that the SATT was suppressed by the DC bias voltage [42]. They obtained good-quality THz pulses using twin photoconductive antennas separated by 500 µm from each other on one substrate instead of using an SATT [43]. They used optical pulses generated by a Michaelson interferometer, but in the present study, optical pulses guided by a fiber with a twin core were used, which was created based on Jordens' method, as shown in the inset in figure 4-3. The cores of custom-built fiber were separated by 256 µm from each other. Two photoconductive antennas are

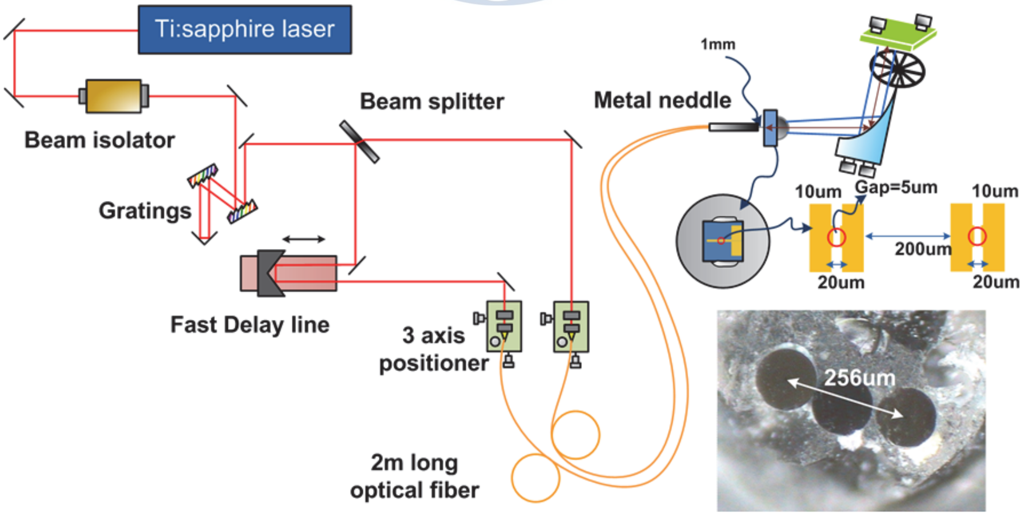

Figure 4-3 Experimental setup for TATT with twin core optical fiber.

separated by 250 µm from center to center on one LTG-GaAs substrate. One of them is a Tx antenna and the other is an Rx antenna. The chip was attached to the center of an Si lens with 10-mm diameter and 6.5-mm height by epoxy adhesive. The experimental setup is shown in figure 4-3, and the measured THz pulse using the fabricated TATT is depicted in figure 4-4. The obtained SNR is 790:1, and the SNR value is large enough for

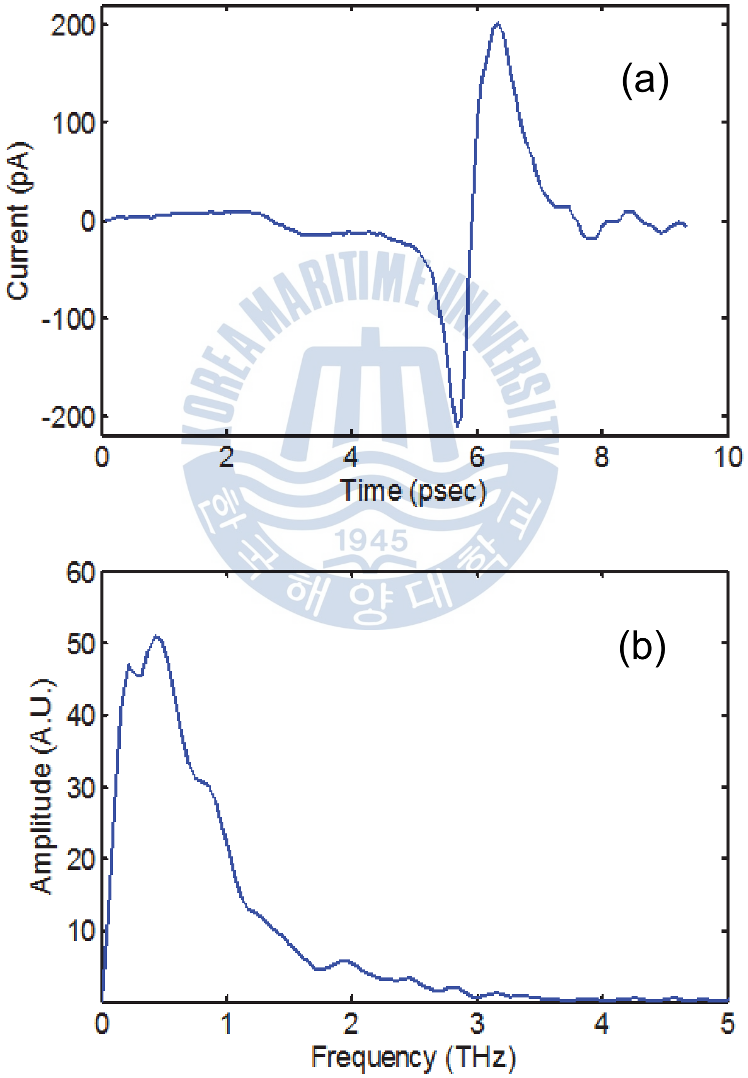

Figure 4-4 (a) Measured THz time domain signal by the TATT (b) Spectrum of (a).

use in *in-vivo* applications.

However, the SNR value is obtained when the optical chopper is located in the path of the THz wave, as shown in figure 4-3, and this chopping method cannot be used in practical applications. If the optical chopper is located in the path of the Tx beam, the Rx antenna is still suppressed by the DC bias voltage, even when the antennas are 250 µm apart from each other, such that high SNR could not be obtained. The same result was revealed when AC voltage was used.

The chopping problem was solved in an unexpected situation. A fast scanning technique should be used in applications for the human body, as mentioned Chapter 1, in order to reduce the measurement time. Because a lock-in amplifier is not needed in the fast scanning method, where a low-noise current amplifier is used, the optical chopper and AC voltage are not needed. The THz pulse could be measured by the TATT using the fast scanning method, thus solving the problems of using an optical chopper and slow measurement time.

The obtained THz pulse using the fast scanning method without an optical chopper is shown in figure 4-5. Unwanted noise is caused by not using the lock-in amplifier, as shown in figure 4-6. The spectrum is the Fourier transform of the signal measured in real time. The velocity of the fast time delay line was 1 mm/s, and the sampling frequency was 1 KHz. There is 60-Hz, 100-Hz, and 125-Hz noise caused by the electric power source, and very-low-frequency noise. The low-frequency noise component is assumed to be due to the thermocouple effect. Although the fast scanning method is

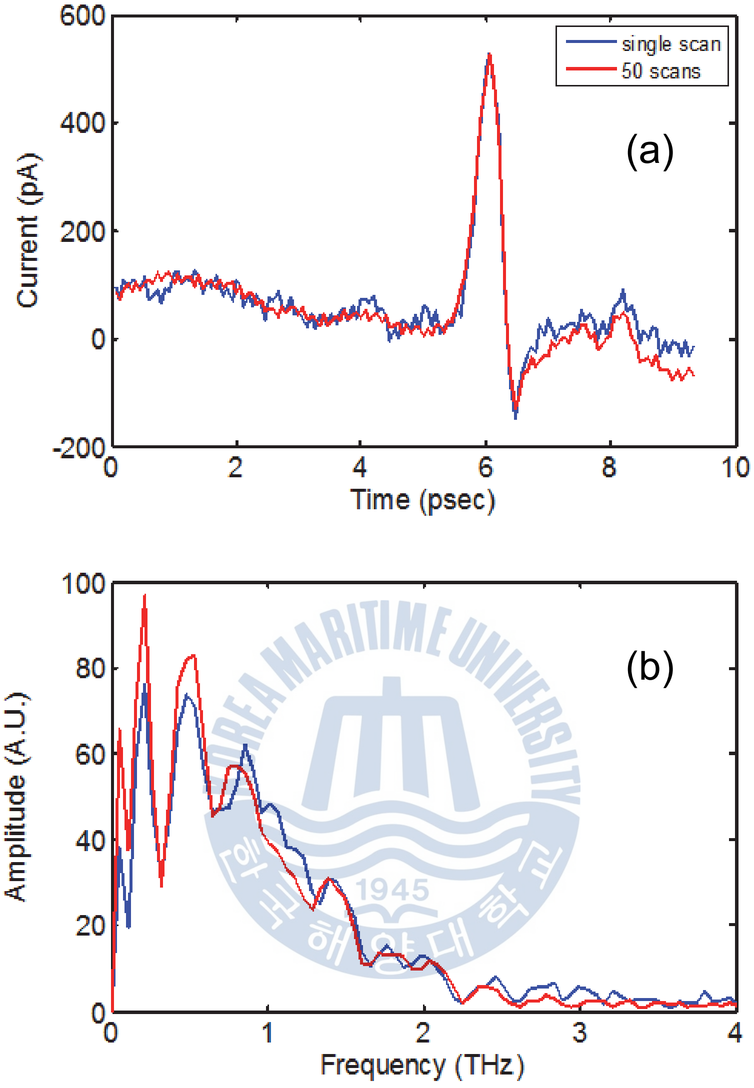

Figure 4-5 Measured THz signal by the TATT with fast scanning.

used without a lock-in amplifier, the THz signal measured by the TATT is much better than that of the SATT using the slow scanning method with a lock-in amplifier. Using the velocity of the fast scan delay line and sampling frequency, the measured real-time data can be converted to the picosecond time scale. The converted time interval between measured data

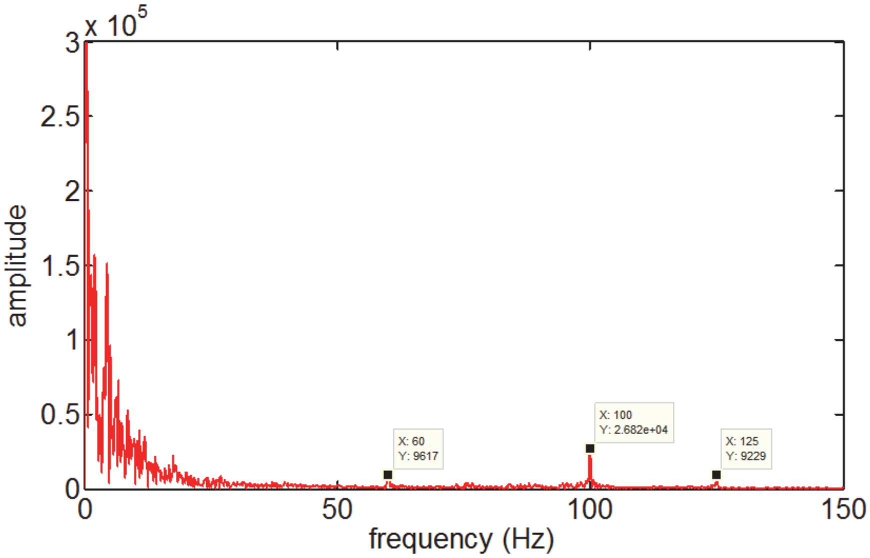

Figure 4-6 Noise spectrum of fast scanning measurement

points was 3.33 fs. The converted time-domain THz pulse is shown in figure 4-5 (a). The solid red line is single-scan data, and the solid blue line is the averaged data of 50 scans. The SNR was reduced compared with that of the THz pulse measured using the slow scanning method with an optical chopper (the pulse is shown in figure 4-4). However, dozens of THz pulses per second can be measured using the fast scanning method without an optical chopper. A THz pulse that is good enough to analyze human body samples is obtained by only a single scan, and the SNR can be increased by averaging the measured THz pulses as shown in figure 4-5 (a).

In this experiment, though a relatively large Si lens with 10-mm diameter was used, the same result will be shown as when a 4-mm diameter Si lens is used. Even if there are several minor problems following miniaturization, these problems can be easily overcome judging from the previous experiment.

4.4 Suggestion for SMTES without DC voltage

4.4.1 Lateral photo-Dember effect

It has been demonstrated that an SMTES can be applied with the fast scanning method without an optical chopper and miniaturized. However, the noise from DC bias voltage still remains, as shown in figure 4-5. Therefore, a method is proposed for manufacturing an SMTES without bias voltage, which is the main cause of noise signals. As mentioned, optical rectification methods and surface emission methods do not need bias voltages. So, the surface emission method is applied to a new SMTES without DC bias voltage. The surface emission method can originate from the acceleration of carriers by a surface depletion field, and by the photo-Dember effect from the difference of carrier mobility between holes and electrons. The generated transient photocurrent caused by these two phenomena flows in the normal direction due to the dipole moment formed in this direction. In order to efficiently radiate the generated THz pulse by the surface emission method to free space, an incident laser pulse is typically applied at 45 degrees, and then the output THz pulse is radiated at 45 degrees from the surface [44-45]. This radiated THz pulse is coupled out very efficiently when the surface is excited at less than 45 degrees. However, a calculation of the total emitted intensity of an effective dipole oriented under 45 degrees to the surface compared to the intensity of a dipole oriented parallel to the surface yields a ratio of 1/2, including the consideration of the total internal reflection [46]. Hence, the 45-degree geometry limits the efficiency of THz emitters based on photo-Dember polarizations oriented perpendicular to the surface. A better out-coupling efficiency can be obtained if the carrier gradient is oriented parallel to the excited surface, because the transient dipole in this case is oriented parallel to the surface [47-48]. This method is called the lateral photo-Dember effect (LPDE). The generated THz pulses can be radiated in the direction normal to the surface using LPDE. In figure 4-7 (a), the principle of THz generation by a typical photo-Dember effect is depicted, and the principle of THz generation by LPDE is depicted in figure 4-7 (b). As the incident laser pulses illuminate the edge of the metal pad, half of the laser pulses are shadowed by the metal pad, and the other half is absorbed by the semiconductor. The absorbed laser pulses generate carriers as shown in figure 4-7 (b). A carrier gradient parallel to an excited surface is easily induced by partially shadowing the excitation area. As LDPE is applied to the SMTES, a relatively high SNR of the THz pulse can be obtained due to the reduced noise by the absence of a bias voltage.

The primary study of THz generation by LPDE was reported in 2009, and there have been a few application studies, but there is a lack of basic

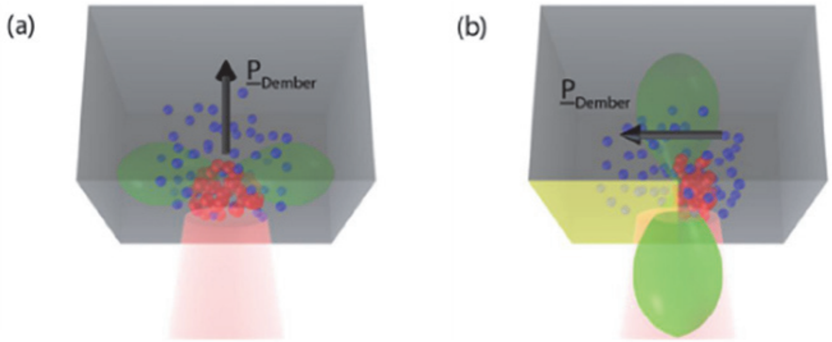

Figure 4-7 (a) Principle of the THz emission from general photo-Dember currents. (b) Principle of the THz emission from lateral photo-Dember currents [47].

information on THz generation by LPDE. The basic study of THz generation by LPDE for SMTES without bias voltage is carried out using InGaAs substrate, which is used in the primary study of THz generation by LPDE. Fortunately, such study can be carried out using various InGaAs samples supplied by Dr. S. K. Noh at KRISS (the Korea Research Institute of Standards and Science).

4.4.2 THz generation dependent on the substrate materials

The intensity of THz generation by LPDE is determined by the difference in carrier mobility of holes and electrons. Three different InGaAs samples with different carrier concentrations, as well as SI-GaAs and undoped GaAs, were used to determine the best semiconductor substrate for THz generation.

Sample	Carrier concentration (1/cm^3)	Mobility (cm^2/V.s)
(AXT) SI-GaAs (KRISS wafer,EPD:1500)	1e9	5000
Undoped GaAs (By MBE,KRISS)	6.3e14	400
Undoped(u) HT-InGaAS	1.1e16	4400
Si lightly doped (n) HT-InGaAS	8.8e16	6100
Si heavily doped (n+) HT-InGaAs	9.8e17	4100

Table 4-1 Various samples for THz generation by LPDE

The carrier concentration and electron mobility of samples are shown in table 4-1, and the measured THz pulses generated by LPDE are depicted for different samples in figure 4-8. The best substrate among these samples for THz generation by LPDE was undoped HT-InGaAs, so all experiments for THz generation by LPDE were carried out using this substrate. The inset figure in figure 4-8 shows the illumination position on the substrate.

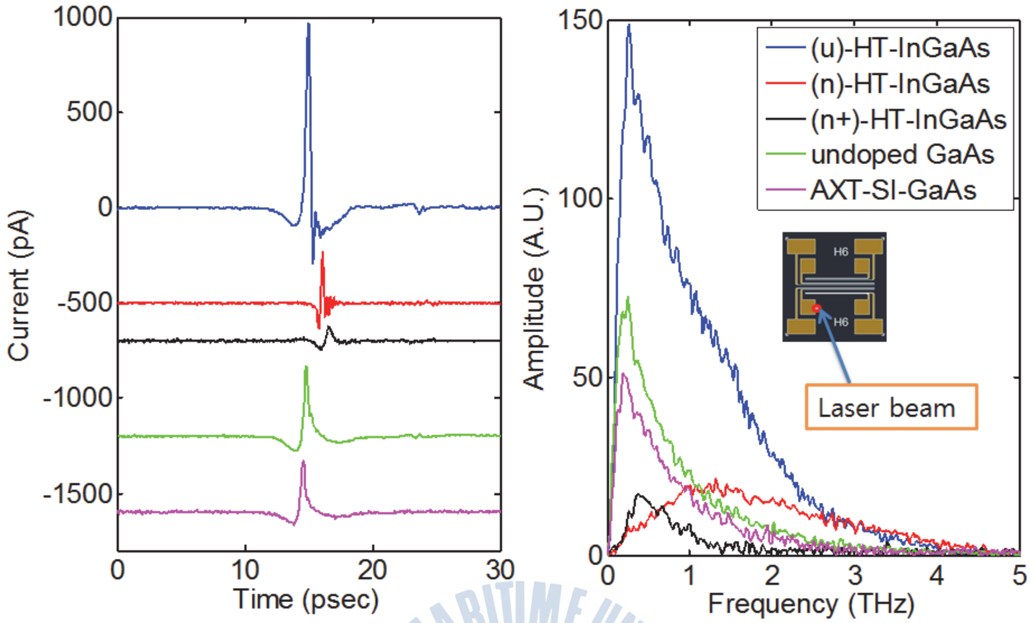

Figure 4-8 Measured time domain THz signal and spectrum

4.4.3 THz generation dependent on the laser beam power

The generated intensity of THz pulse was investigated for different laser beam powers. The laser beam power is changed from 6.2 mW to 125 mW, and a 5-10-5 Rx photoconductive antenna on LTG-GaAs substrate was used. The measured THz time-domain signal is depicted in figure 4-9, and the measured peak-to-peak amplitude is shown for different laser beam powers in figure 4-10. The intensity of THz pulses generated by LPDE increased with increasing laser beam power. However, the slope of THz generation became smaller with high laser beam power, as shown in figure 5-10. The inset graph in figure 5-10 shows the measured noise signal for laser beam power of 6.2 mW and 125 mW. The calculated RMS values of noise signals are 1.32 pA and 1.52 pA, respectively. Although the laser beam

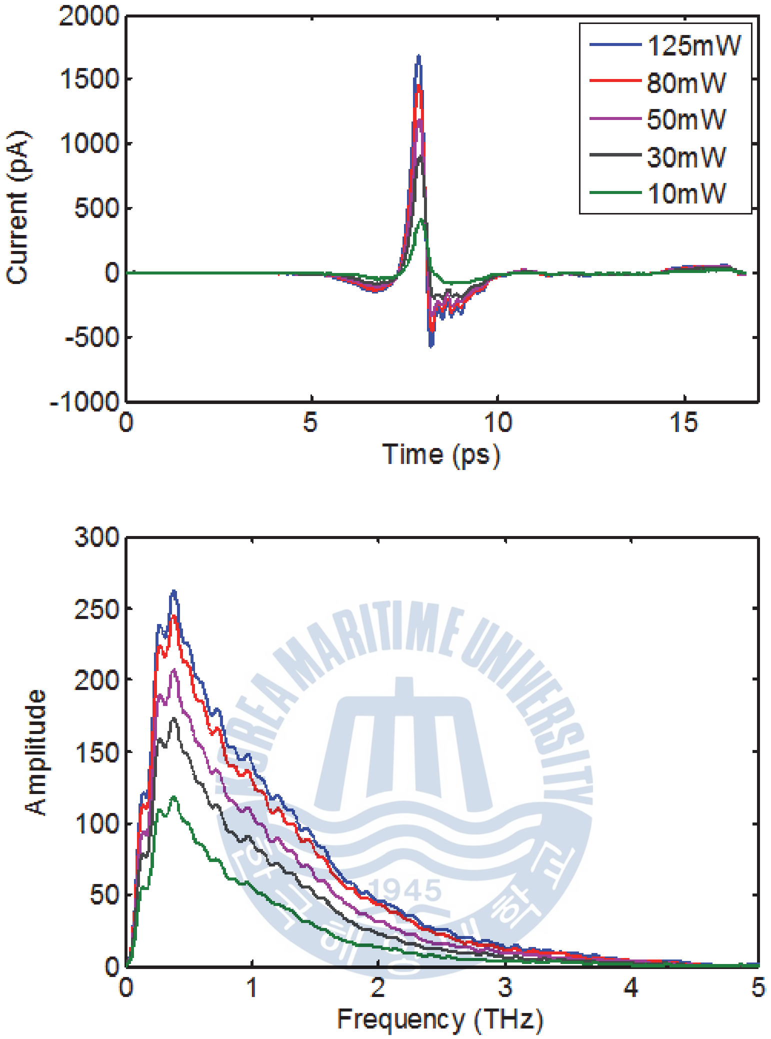

Figure 4-9 Measured THz time domain signal and spectrum dependent on the irradiated laser beam power.

power was increased 20 times, the noise signal was almost the same. Accordingly, the calculated SNR is 5 times improved, from 198:1 to 1080:1. A better SNR was obtained after removing the bias voltage, which is the main cause of noise. The SNR measured by the SMTES with the fast scanning method will be improved by applying LPDE.

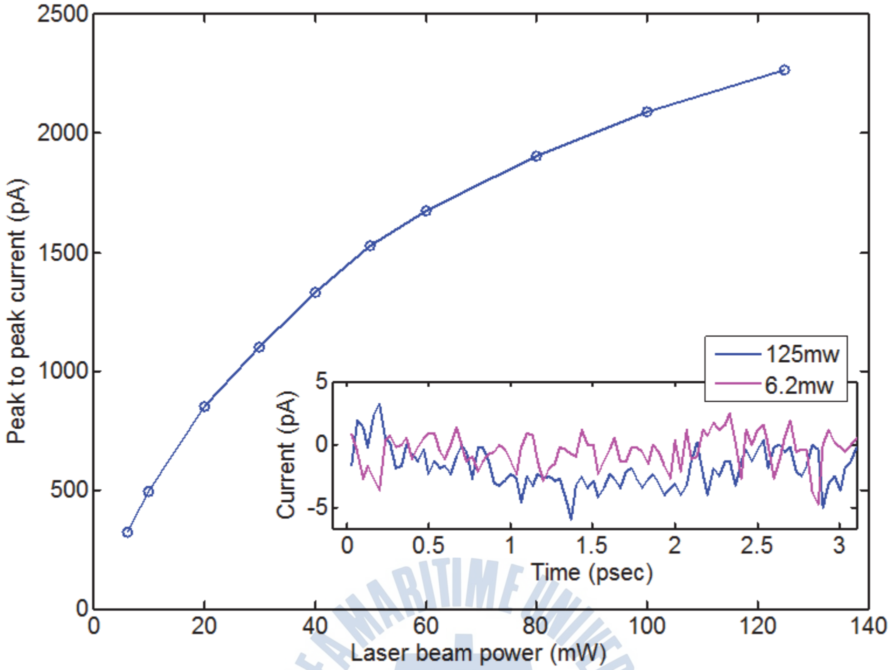

Figure 4-10 Peak to peak value of measured THz time domain signal dependent on the irradiated laser beam power.

5. Novel THz otoscope

The fundamental reason for using THz waves for cancer diagnosis is that THz waves interact sensitively with water molecules. In this chapter, another THz medical device with large expected ripple effect has been fabricated using this property of distinguishing water molecules: a THz otoscope (TOS) that can diagnose otitis media by objective data (THz signal). Otitis media collectively include everything that happens within the middle ear with inflammatory changes. The otitis media accompany organic changes in the middle ear cavity, the mucous membrane of the middle ear and epithelial cells, and signs of bone destruction of the middle ear structure. The existing diagnostic methods for otitis media verify the existence of tympanic membrane perforation and pus in the middle ear using optical otoscopes, or surgery optical microscopes. However, when changes to cells and organs are verified by optical methods, the progression of the disease has already significantly progressed. Moreover, because the diagnosis is done based on a physician's clinical experience, the diagnostic accuracy of otitis media depends on the ability of the doctor. Impedance audiometry is a diagnosis method for otitis media based on objective data, it has difficulties with diagnosis standardization, and must be performed by an audiometry expert. The TOS has potential for easy standardization and for operation by doctors who do not know about THz techniques. THz waves can be used to check for the presence of water molecules. The common symptoms of otitis media are accompanied by inflammation, which is characterized by high water content. Accordingly, the TOS can objectively diagnose otitis media by identifying the presence of inflammation using THz waves. The TOS was manufactured by combining a commercial otoscope and a THz module, which can generate and detect THz waves.

5.1 Design of THz otoscope (TOS)

The ear is separated into the external ear, middle ear, and inner ear. In order to diagnose otitis media, the THz waves radiated from a TOS travel through the tympanic cavity, whose length is 30~35 mm and diameter is 7~9 mm. Then, the THz waves should be measured by the TOS after reflecting from the tympanic membrane. The TOS was designed by combining a commercial otoscope and a THz module. The THz module used in the TOS is an MTES type, in which the Tx and Rx are separated.

The experimental setups for fabricating a TOS and commercial otoscope are shown in figures 5-1 and 5-2 respectively. The TOS was designed as two types. One type is an angled TOS (ATOS) type, as shown in figure 5-1 (a),

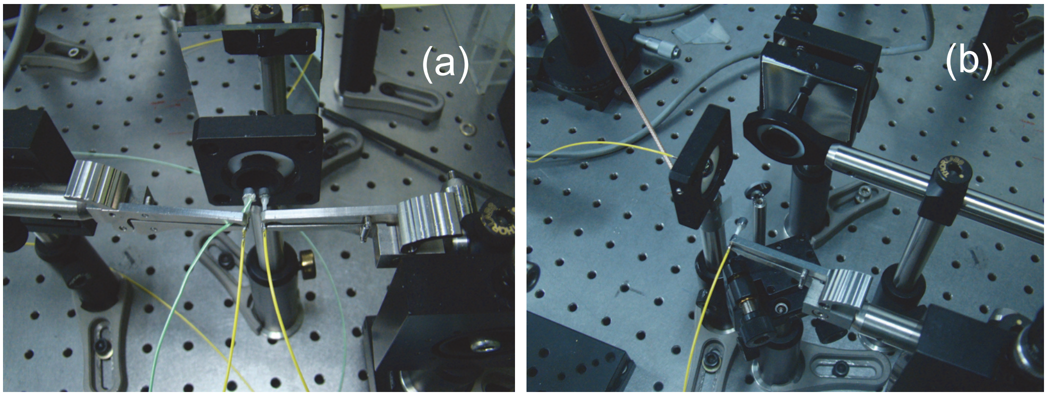

Figure 5-1 (a) Experimental setup for anlged TOS. (b) Experimental setup for interferometric TOS.

Figure 5-2 Photograph of commercial otoscope.

and the other is an interferometric TOS (ITOS) type, as shown in figure 5-1 (b). The ATOS can detect larger THz signals compared with the ITOS, because there is no loss of THz waves other than the loss by the aperture at the end of the otoscope. However, the ATOS has disadvantages in that the position must conform to the focal point determined during the fabrication process, and the incident THz pulse must illuminate the tympanic membrane at an angle.

The ITOS complements the ATOS. The ITOS is designed in the form of an interferometer, and the incident angle of the THz waves to the tympanic membrane is thus zero, and the ITOS is independent of the focal length. However, there is a 60% loss of incident THz intensity, which is caused by Fresnel loss by using the interferometric type. Two forms of the TOS have been fabricated, and their properties have been reported.

5.2 Design of Si lens for TOS

5.2.1 Si lens for ATOS

Because the THz module should be combined with a relatively small otoscope without obstructing the sight of the doctor, the design of the Si lens is very important for manufacturing a TOS. The Si lens is designed to have minimum reflection or scattering loss, which is caused by a hole at the end of otoscope, and to efficiently radiate and detect THz waves. A commercial otoscope is combined with a THz module, and modeled by AutoCAD and depicted with the MTES, as shown in figure 5-3.

The otoscope used is a *Piccolight* made by the KaWe company in Germany. The total path length of a moving THz wave is 130 mm, and the 6-mm-diameter holes at the end of the otoscope are located at 40 mm and 90 mm in the moving path of THz waves. The hole positions are notated as 1 and 2, as shown in figure 5-3. The Rx position of the MTES is notated 3. When the focal position of the optical lens on an otoscope is

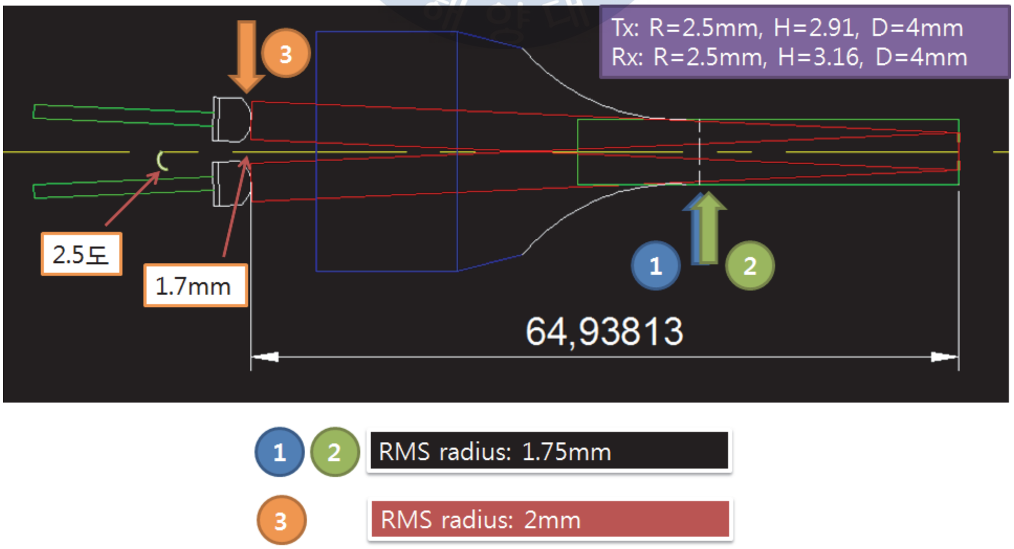

Figure 5-3 Modeling of ATOS with commercial otoscope by Autocad.

assumed as the position of the tympanic membrane, and the loss by the 6-mm-diameter hole was considered, the final form of the ATOS includes an angle between the Tx and Rx modules is 2.5 degrees, with 1.7-mm separation from each other. The radius of curvature of the high-resistivity Si lens is determined as 2.5 mm, and the diameter is determined as 4 mm.

The Si lens was designed by considering this radius of curvature and diameter. In figure 5-4, the simulation results obtained using Zemax software based on the ray trace method is shown. The form of electromagnetic radiation by the dipole antenna is widely known, and is shown in figure 5-5. As the angle of the optical axis was considered as 0 degrees, most of

Figure 5-4 Result of Si lens design by Zemax simulation program

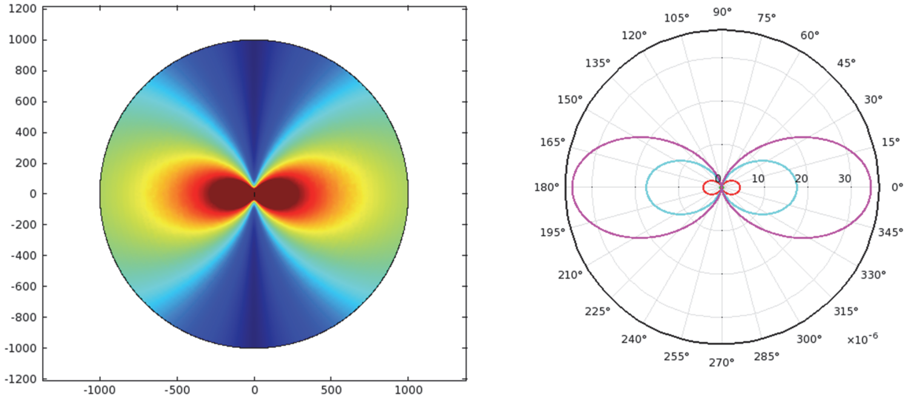

Figure 5-5 Radiation pattern of general dipole antenna

the energy of the electromagnetic waves is radiated under 45 degrees. Therefore, the angle of THz radiation was set as 45 degrees in the Zemax simulation. When the THz waves pass through positions 1 and 2, the radiated THz waves with large angles of 35~45 degrees are blocked by the 6-mm-diameter hole. However, most THz waves under 35 degrees arrived at the Rx THz module. The beam waist of the radiated THz waves under 35

H of Si lens	RMS radius at 40mm (at 34 degree)	90mm(at 34 degree)	130mm(at 34 degree, 36degree)	200mm(at 34 degree)	300mm(at 34 degree)
2.88mm	1.76mm(1.2, 2.15)	2.56mm	3.24mm(3.16mm)	4.44mm	6.19mm
2.90mm	1.43mm	1.92mm	2.40mm(2.44mm)	3.30mm	4.67mm
2.91mm	1.27mm	1.66mm	2.10mm(2.28mm)	3.00mm	4.39mm
2.92mm	1.20mm	1.47mm	1.96mm(2.32mm)	2.98mm	4.54mm
2.93mm	0.98mm	1.39mm	2.00mm(2.54mm)	3.24mm	5.10mm
2.94mm	0.85mm	1.43mm	2.22mm(2.92mm)	3.74mm	5.96mm
2.95mm	0.75mm	1.60mm	2.58mm(3.39mm)	4.39mm	7.02mm
2.98mm	0.73mm	2.53mm	4.09mm(5.16mm)	6.85mm	11mm

Table 5-1 RMS radius of THz beam dependent on the distance from Tx.

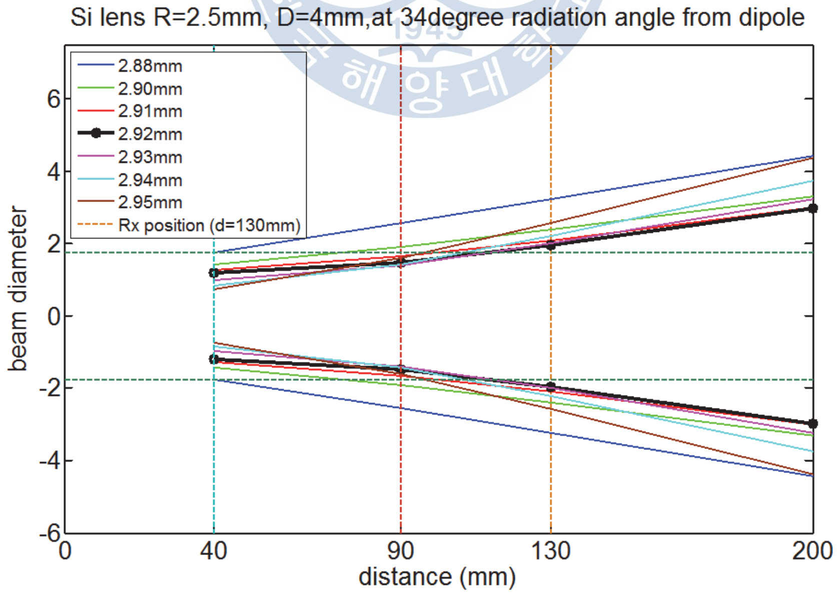

Figure 5-6 THz beam divergence dependent on the height of Si lens.

degrees should be smaller than 4 mm in diameter for lossless propagation. The RMS radius of THz waves depending on The height of the Si lens is shown table 5-1, and the beam waist of THz waves depending on the propagated distance is depicted in figure 5-6. The optimal height of the Si lens of Tx was found as 2.92 mm by Zemax simulation. The optimal height of the Si lens of Rx was determined as 3.16mm.

5.2.2 Si lens and window for ITOS

The design of the Si lens for ITOS was progressed in the same way as that of ATOS. In an interferometric system, an additional Si window is needed, unlike in ATOS. This Si window is operated as a beam splitter in optics. The amplitude of THz waves transmitted and reflected in the Si window is easily determined by the Fresnel diffraction formula. The final intensity of THz waves acquired by ITOS is only 38% of the incident intensity, but there is an advantage in that the incident angle to the tympanic membrane is 0 degrees. The diameter of the Si window used is 12 mm, and the thickness is determined as 1.5 mm. The position of the second THz pulse by internal reflection in the Si window is determined by the thickness of the Si window, and the second pulse appears after 34 ps when the thickness is 1.5 mm, indicating that the Si lens is suitable for ATOS, because the time interval between the first pulse and second pulse is appropriate. The designed height of the Tx Si lens is 2.92 mm, the radius of curvature is 2.5 mm, and the diameter is 4 mm. The designed height of the Rx Si lens is 6.5 mm, the radius of curvature is 5 mm, and the diameter is 10 mm.

5.3 Use of ITO glass

Both types of TOS were designed using a THz module with optical diagnosis by a doctor. In order to do so, a material that is transparent in the visible regime and metalized in the THz regime for total reflection should be used. The material used for TOS is indium tin oxide (ITO) glass. ITO is a solid solution of indium(III) oxide (In_2O_3) and tin(IV) oxide

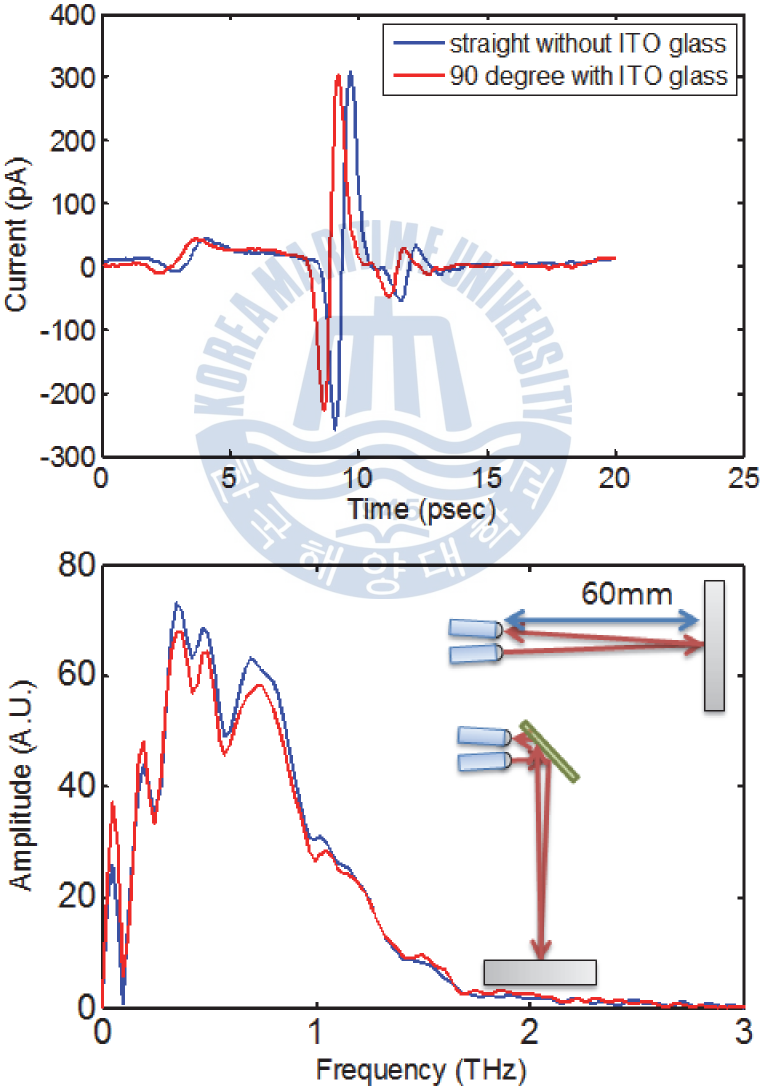

Figure 5-7 Measured THz signal with and without ITO glass.

(SnO_2), typically composed of 90% In_2O_3 and 10% SnO_2 by weight. It is transparent and colorless in thin layers, while in bulk form, it is yellowish to grey. In the infrared region of the spectrum, it acts as a metal-like mirror. ITO glass is made by the vacuum deposition of ITO on glass. The sheet resistance of ITO glass depends on the thickness of the ITO thin film. The sheet resistance of the ITO glass used for the TOS is 10 Ω/sq with 200-nm thickness of the ITO thin film. The reflected THz pulse from the metal plate with and without ITO glass is depicted in figure 5-7. The measured peak-to-peak amplitude of the THz pulse without ITO is 562.3 pA, and that of the THz pulse with ITO is 524.8 pA. The calculated efficiency using ITO glass is 93%.

5.4 Measured THz signal by manufactured TOS

The obtained THz pulses using the fabricated ATOS and ITOS are depicted in figures 5-8 and 5-9, respectively. The peak-to-peak amplitude of the THz pulse by ATOS and reflected from a metal plate is 300 pA, and the spectrum extends up to 2 THz, as shown in figure 5-8. The peak-to-peak amplitude of a THz pulse by ITOS reflected from a metal plate is 190 pA, and the spectrum extends up to 1.5 THz, as shown in figure 5-9. The ringing component between 0.2 THz ~ 0.3 THz is caused by diffraction of the low-frequency component. The ringing can be reduced using a graphite sheet, which produces scattered reflection. When the otoscope is used in practical applications, an additional apparatus is used, an ear tip, which helps facilitates a doctor's sight of the tympanic membrane. The ear tip is

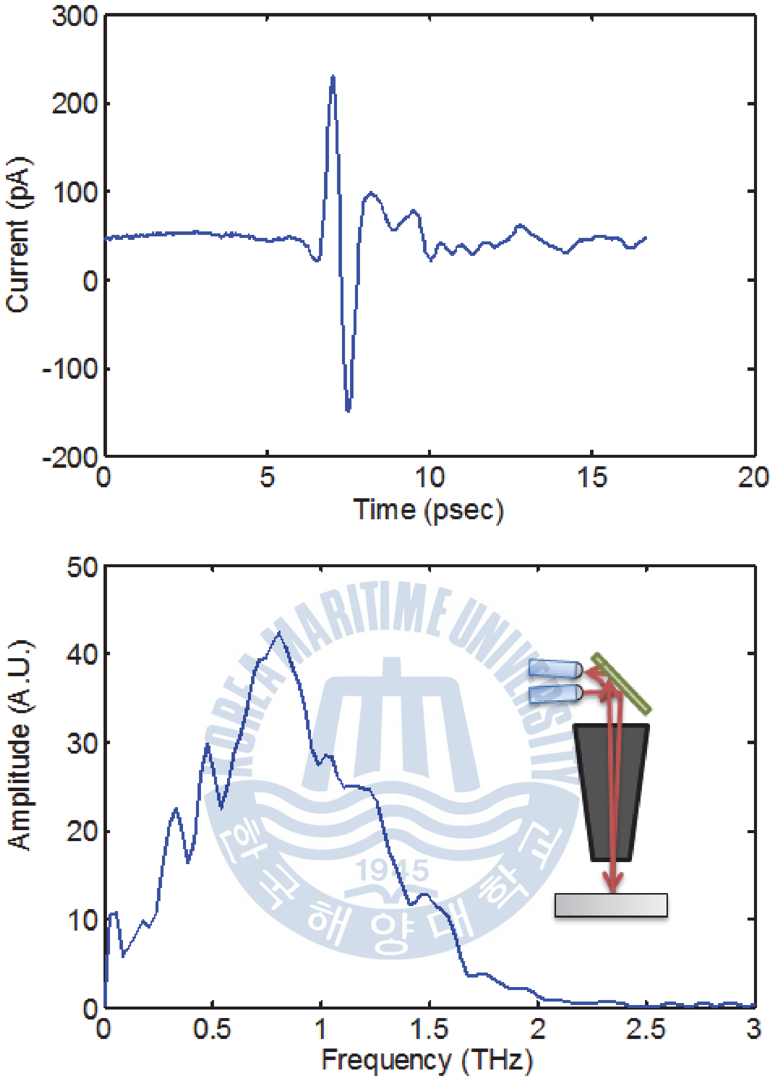

Figure 5-8 Measured THz signal by the manufactured ATOS.

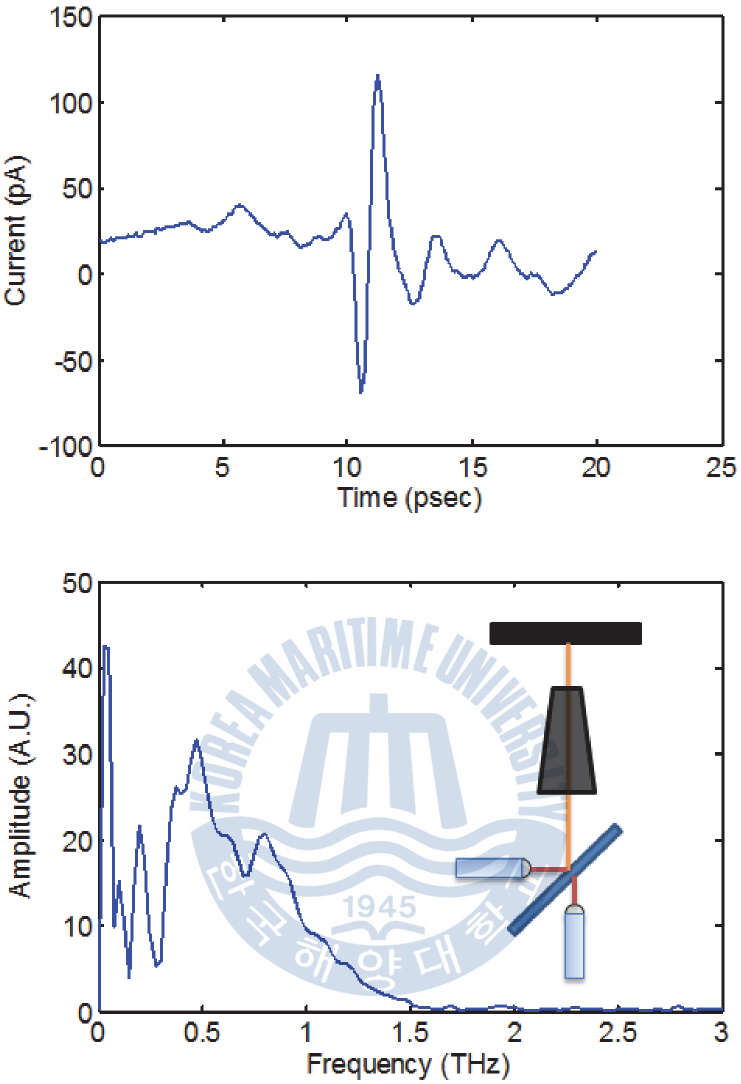

Figure 5-9 Measured THz signal by the ITOS.

made by a line of a plastic such as sanalon. The ear tip used for the TOS in this study is a sanalon ear tip made by the Heine company. The ear tip diameter gradually decreases at 8.3 degrees, and the diameter at the end of tip is 5 mm, as shown in figure 5-2. The measured THz signal with an ear tip reflected from an Al plate located 6 mm from the end of the ear tip is

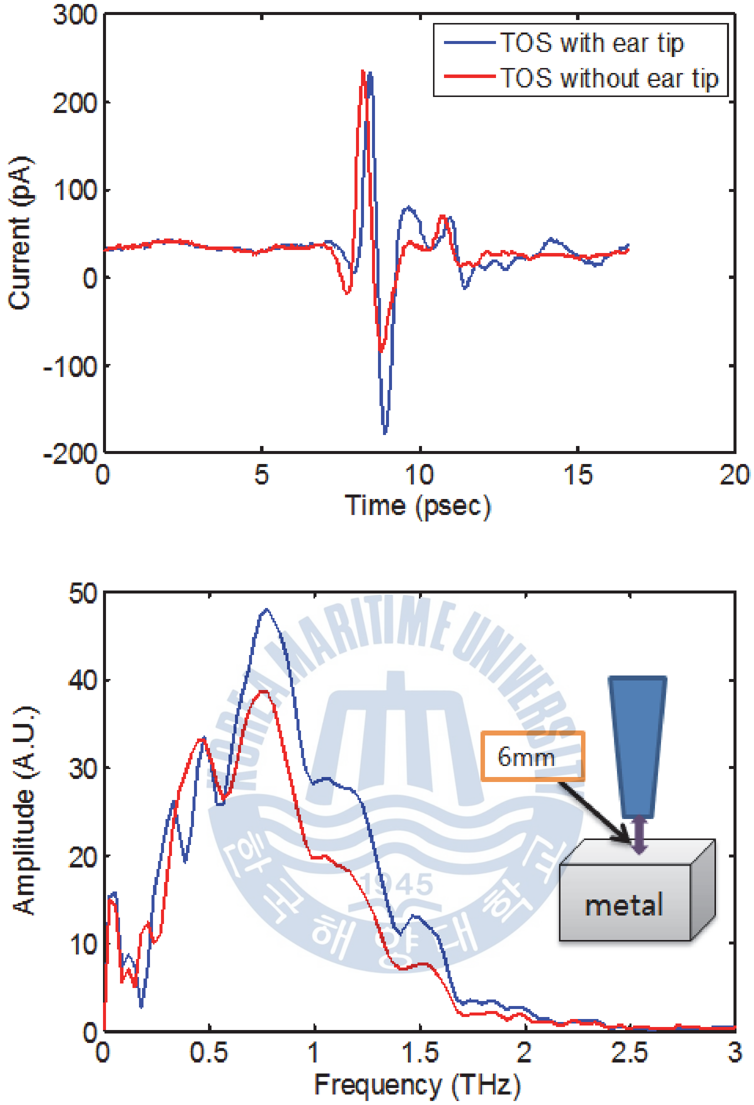

Figure 5-10 Measured THz signal by ATOS with and without ear tip.

shown in figure 5-10. The measured peak-to-peak amplitude is increased 25% using the ear tip. The result is obtained assuming that the diffracted THz pulses are partially guided by the ear tip. For analysis of this result, an in-depth study is required for the THz waveguide domain. The end of the ear tip is moved to the opposite side from the Al metal, after which

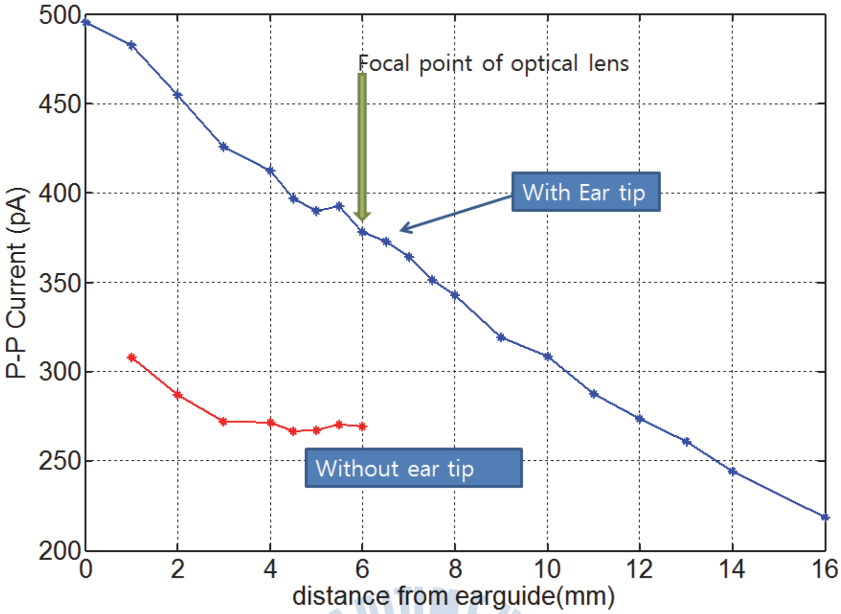

Figure 5-11 Peak to peak value of measured THz signal by ATOS with and without ear tip.

changes to the THz pulses are observed. The peak-to-peak amplitude depending on the distance between the end of the ear tip and the Al plate is depicted in figure 5-11. When the end of the ear tip is in contact with the Al plate, the measured peak-to-peak amplitude is largest. At a distance of 6-mm (the real tympanic membrane position), the peak-to-peak amplitude is 80% compared with the amplitude at the contact position.

5.5 Reflection measurement of thin dielectric film and skin of mouse

5.5.1 Modeling of membrane

In order to practically measure the tympanic membrane of a human body, several problems exist, such as obtaining permission from the KFDA (Korea Food & Drug Administration), and cooperation with skilled physicians.

Therefore, instead of using the tympanic membrane, we indirectly demonstrate that the fabricated TOS can measure a reflected THz pulse from the tympanic membrane by using a thin dielectric film and thin mouse skin.

The tympanic membrane is a thin and transparent membrane with 100-μm thickness, and is located at the interface between the external ear and the middle ear. The membrane is separated into a cuticle layer, a fibrous layer, and a mucous layer. The refractive index of skin and fibrous tissues is 1.9 ~ 2.2 [40,49-50]. The principle of diagnosis of otitis media is distinguishing the presence of water in the inner part of the tympanic membrane. The presence of water in the inner part of the tympanic membrane can be verified by the amplitude and position of reflected THz pulses from the interface between the membrane and samples. The otitis media diagnostic ability is demonstrated using a dielectric film and mouse skin to approximate the tympanic membrane. The demonstration is carried out both experimentally and with numerical simulation.

5.5.2 Reflection measurement from thin dielectric film

The reflected THz pulses from 74-μm dielectric thin film (polyethylene) are measured by ITOS. Reflected THz pulses are measured for samples of air, methanol, and water placed in contact with the thin dielectric film. In the THz regime the refractive index of the dielectric film used is almost constant at 1.55. Although the refractive indices of water and methanol depend on frequency, the refractive indices are 2 and 1.55 at 1 THz, respectively. Therefore, simulation by FDTD is carried out using these

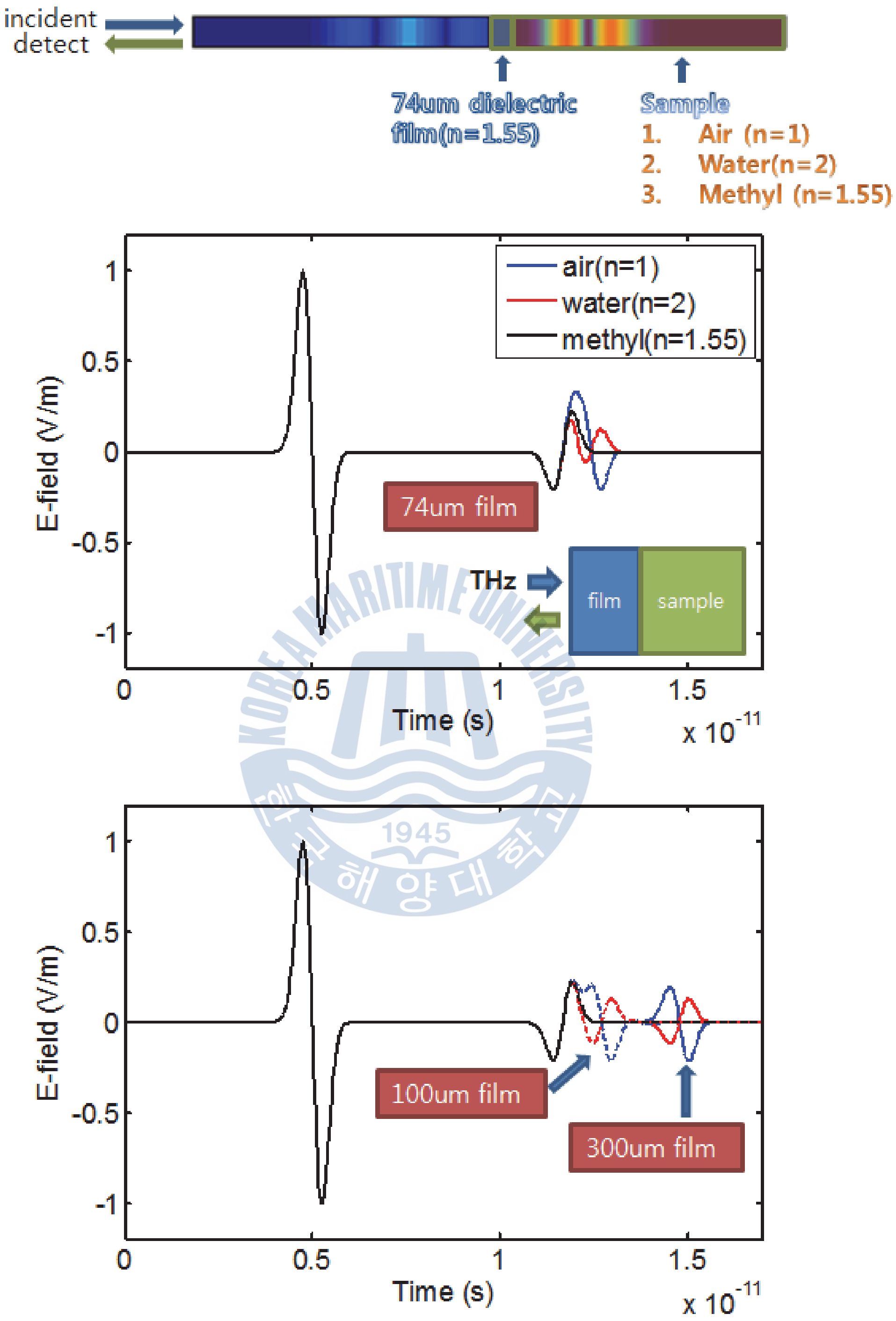

Figure 5-12 2D FDTD simulation of reflected THz signal at the two boundary.

refractive index values. The results are shown in figure 5-12. Simulation results are shown for a dielectric film thickness of 74 μm in figure 5-12 (a). The large THz signal near 0.5ps is the incident Gaussian THz pulse with the 0~2 THz spectrum. The reflected and composed THz pulses are shown near 12 ps for the interface between air and the dielectric film, and that from the interface between the dielectric film and the samples.

Because the thin dielectric film is very thin as 74 μm, the two pulses reflected from the two interfaces were not clearly separated. Therefore, in order to distinguish the two pulses, simulation was carried out using 100-μm and 300-μm-thick dielectric films, as shown in figure 5-12 (b).

The overlapping shape of THz pulses for 100-μm thickness of the dielectric film is similar to that of 74 μm. For a film thickness of 300 μm, the two pulses are clearly separated. The reflected THz pulse from the first interface (air/dielectric film) is the same regardless of samples at the second interface (dielectric film/ samples). On the other hand, the reflected THz pulse from the second interface is changed depending on the samples. The amplitude of THz waves reflected from the sample depend on the difference in refractive indices, and is determined by the Fresnel diffraction formula. The phase of the reflected THz pulse from air is delayed by 180 degrees compared with that from the first interface, and the amplitude is 25% compared with the amplitude of the incident THz pulse. There is no reflection for the methanol sample, because the refractive index of methanol is the same as that of the dielectric film. The phase of the reflected THz pulse from water is the same as that from the first interface, and the amplitude is 12.1% compared with the amplitude of the incident THz pulse. From the analysis, for a dielectric film thickness of 74 μm, the THz pulse reflected from air seems to be due to the combination of two pulses, and the amplitude is large. The THz pulse reflected from water seems to be two THz pulses, although the two

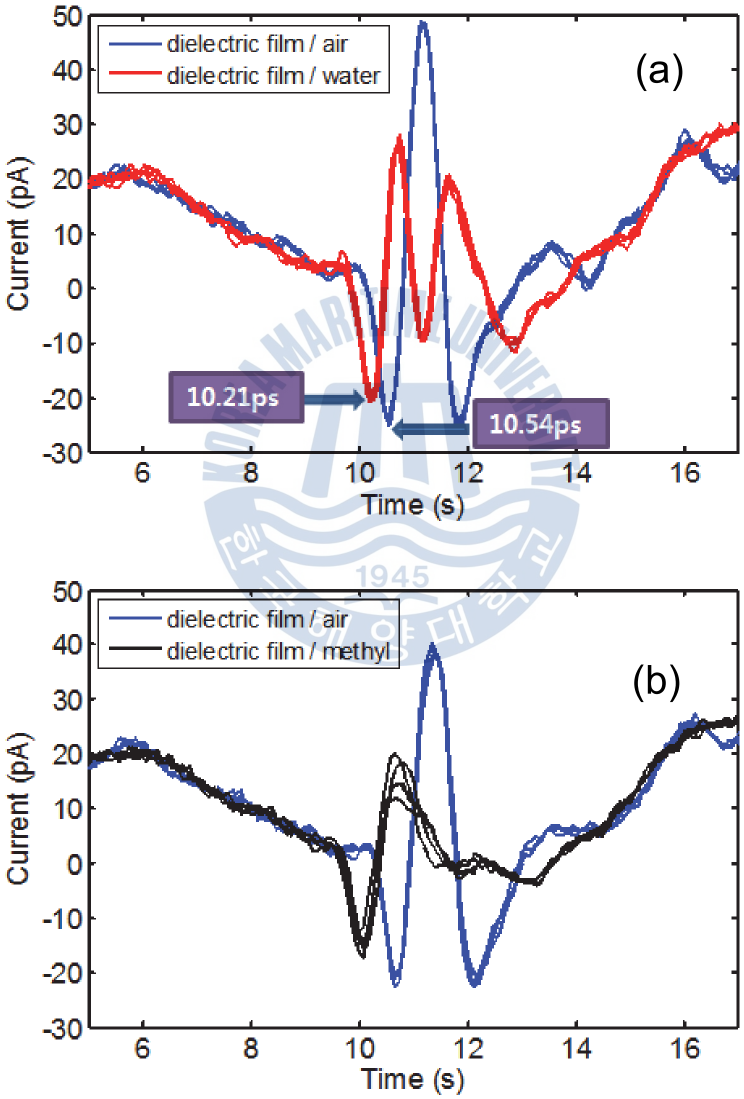

Figure 5-13 Experimental results of reflected THz signal at the two boundary.

pulses were combined. The simulation results show that the presence of water in the inner part of the dielectric film used to model a real tympanic membrane can be distinguished. A practical experiment is carried out with similar conditions, and the THz pulses reflected from air and water are depicted in figure 5-13 (a). Similar to the simulation results, the reflected THz pulse from air is shown as a large THz pulse, and the reflected THz pulse from water is shown as two pulses. The position of the reflected THz pulse from the first interface when the sample is water is changed, because the dielectric film position is moved to the TOS by the pressure of the water. The reflection from the first interface should appear in the same position according to the simulation results. Therefore, the moving distance of the dielectric film can be calculated by the time interval as 99 μm. A reflected THz pulse from the second interface when the sample is methanol is not detected, as shown in figure 5-13 (b).

5.5.3 Reflection measurement from mouse skin

Assuming that the properties of the tympanic membrane are similar to those of human skin according to the opinion of a doctor, the refractive index of the tympanic membrane is also similar to that of skin. Accordingly, another experiment was carried out using mouse skin, which is used to model the tympanic membrane. An experiment was carried out with the YUHS-KRIBB medical convergence research institute. All experiments were conducted with the approval of the Association for Assessment and Accreditation of Laboratory Animal Care (AAALAC) International.

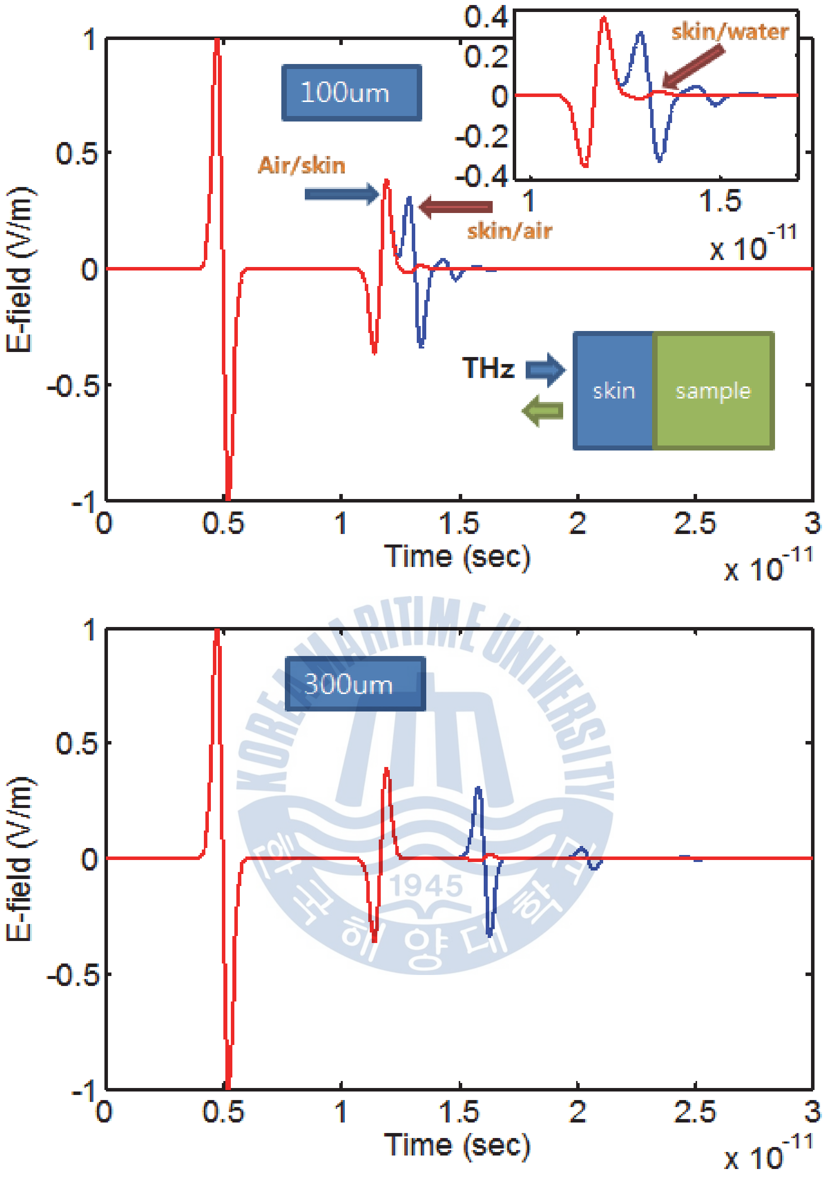

Figure 5-14 Experimental results of reflected THz signal at the two boundary (skin/sample).

First, in order to predict the experimental results, FDTD simulation was carried out. The refractive indices of mouse skin, water, and air were set to 2.19, 2.27, and 1, respectively at 0.5-THz frequency. The simulation results

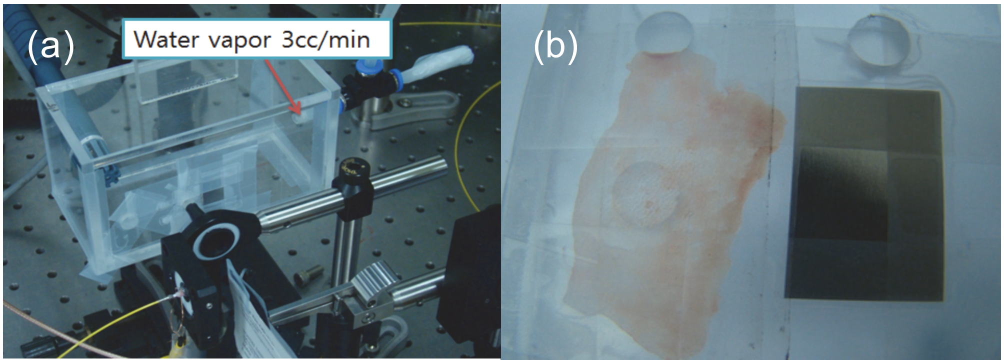

Figure 5-15 (a) Experimental setup for reflection measurement from mouse skin (b) Photograph of mouse skin and metal.

are depicted in figure 5-14. In order to distinguish two pulses, the thickness of the mouse skin was set to 100 µm and 300µm. The reflected THz pulse is overlapped when the thickness is 100 µm. The refractive indices of mouse skin and water are similar, and there is no reflection from the second interface when the sample is water. The reflected THz pulse from the second interface is large due to the large difference in refractive indices when the sample is air. The simulation results show that the presence of water in the inner part of the mouse skin used to model a real tympanic membrane can be distinguished.

The setup of the reflection experiment using mouse skin is shown in figure 5-15 (a). The experiment was carried out using ITOS alone before the final combination for ease of experimentation. Real mouse skin and an Al metal plate is shown in figure 5-15 (b). In order to supply the water molecules quantitatively to the inner side of the mouse skin, an acrylic chamber was made. The changes of the reflected THz pulse while supplying 3 cc per minute of water molecules was observed, and figure 5-16 shows the results.

While the water molecules were supplied for 80 minutes, the reflected THz pulses gradually became smaller as time passed, and were saturated after 80 minutes. The saturated amplitude is 76% relative to the amplitude before supplying water molecules. Like in the simulation results, the difference in the refractive indices between the mouse skin and the sample was reduced,

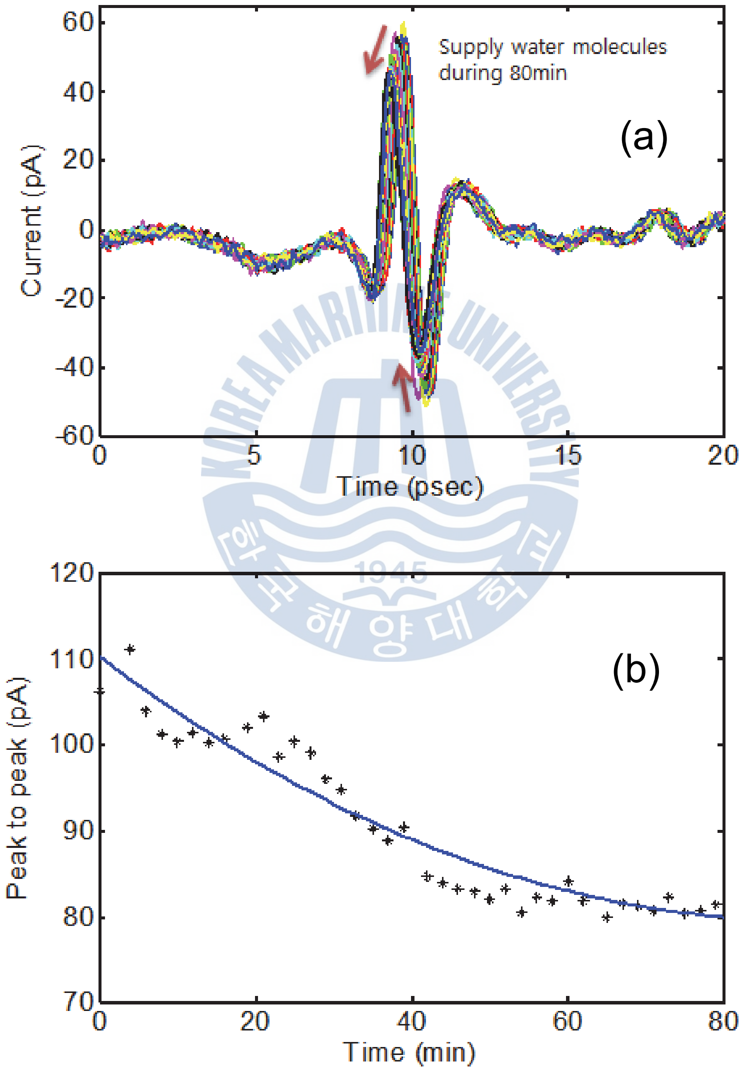

Figure 5-16 (a) Change of time domain THz signal dependent on the water molecules. (b) Change of peak to peak amplitude.

so the reflected THz pulse was also reduced. For clarity, water was supplied to the inner side of the mouse skin using a pipette. There is a hole with 8-mm diameter and 5-mm thickness behind the mouse skin, as shown in figure 5-15 (b), and the water injected into the hole remained due to the surface tension of the water. The measured THz signals are depicted in

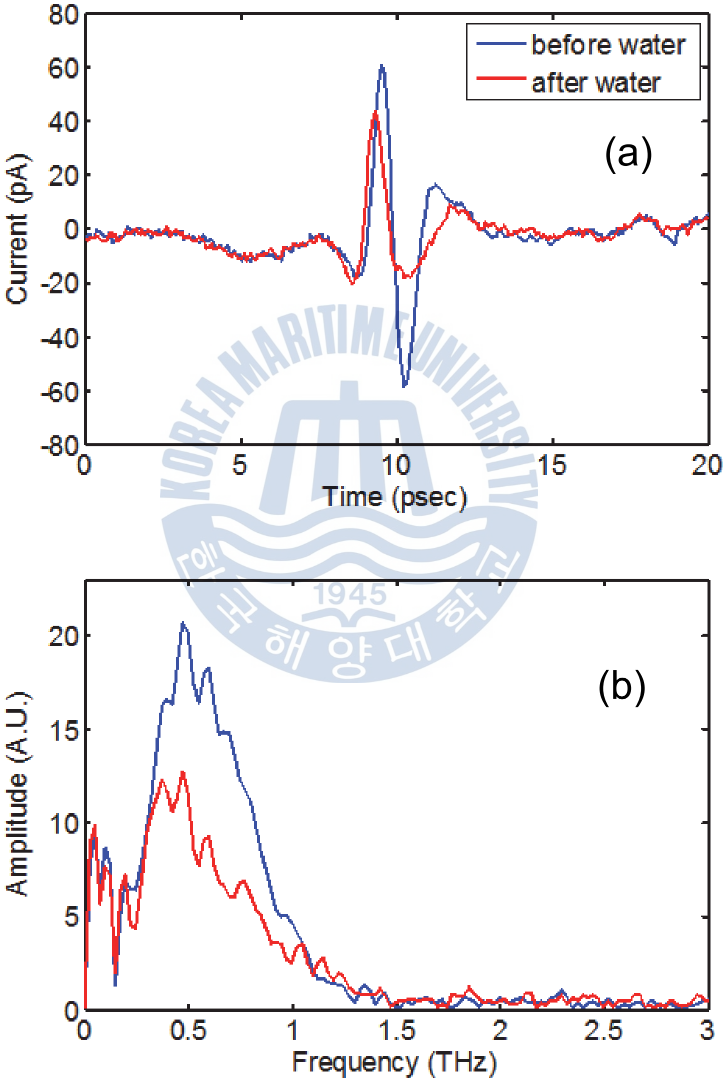

Figure 5-17 Reflection measurement from boundary between mouse skin and sample

figure 5-17.

The reflected THz pulse from the second interface disappeared in the presence of water. The measured thickness of mouse skin is 102 µm, which is almost the same as the simulated thickness. However, the two pulses are explicitly separated in the simulation for the air sample, and the two pulses seem to be a THz pulse in the experiment, although the thickness is almost the same. One of the reasons is the difference in frequency bandwidth between the source of the simulation and the measured THz pulse in the experiment. The frequency of the incident THz pulse used in simulation extended up to 2.5 THz, such that the THz pulse is sharper than the measured THz pulse whose frequency extended up to 1.2 THz. Accordingly, in the experiment, the pulses seemed to be a THz pulse. Another reason is dispersion. The refractive indices of mouse skin depend on the frequency in the THz regime. The refractive indices rapidly increased under 0.5 THz, and the dispersion of the THz pulse is caused by the refractive index, depending on the frequency. When the dispersive THz pulses are combined, the two pulses seem to be a single pulse.

For these two reasons, the measured THz pulses are somewhat different from the simulation results, but the results revealed that the manufactured TOS can detect the presence of water in the inner part of mouse skin. This means that the TOS is adequate for diagnosis of otitis media. Figure 5-18 shows the changes of measured THz pulses for when the water is dried naturally after removing water on the inner side of the mouse skin. The measured THz pulses become lager as the inner side of the mouse skin dries. The capabilities of the TOS are reconfirmed by the results.

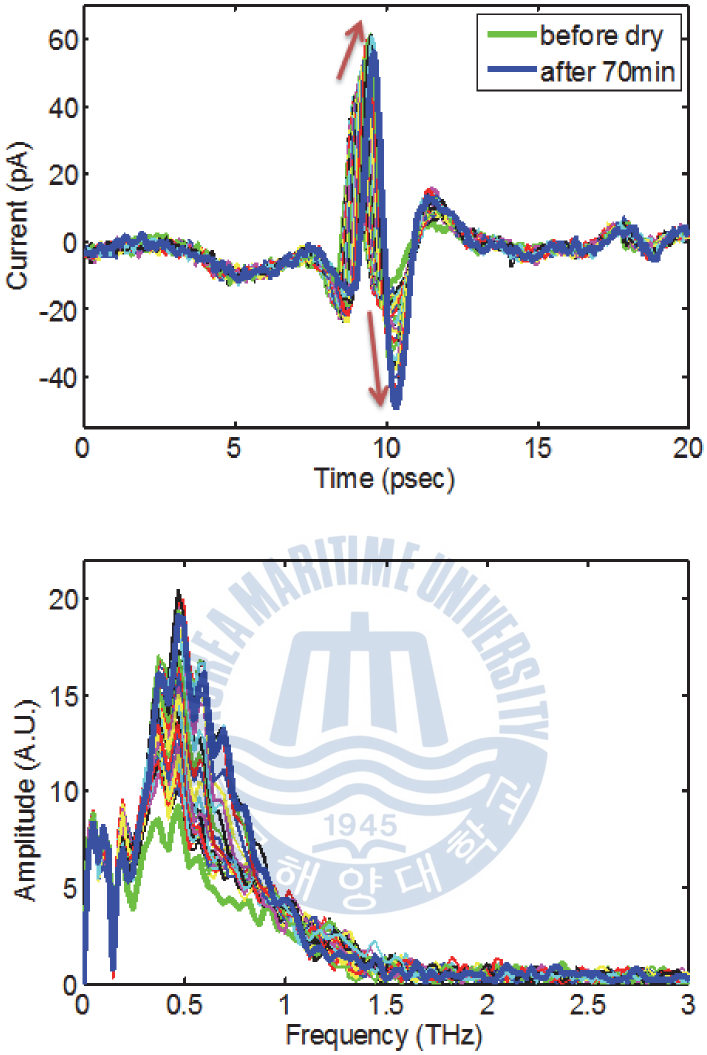

Figure 5-18 Change of THz signal dependent on the water content with natural drying.

5.5.4 Reflection simulations from flat membrane and conic membrane

A practical tympanic membrane is cone-shaped, and is tilted with respect to the external auditory meatus at about 40 degrees. The tilted angle can be compensated for by a doctor, but the cone-shape cannot be compensated.

The effect of the cone-shape structure is confirmed by FDTD simulation. Figure 5-19 (a) shows the modeled structure of the cone-shaped tympanic membrane. Figures 5-19 (b) and (d) show the reflections from the flat-shaped tympanic membrane and the cone-shaped tympanic membrane, respectively. Many portions of the incident THz pulses are reflected to the dislocated direction by the cone structure, as shown in figure 5-19 (d). Although the flat part is only 1-mm in the cone-shaped tympanic membrane, the amplitude of the reflected THz pulses is 33% relative to that from the flat surface, as shown in figure 5-19 (c). It is confirmed that the adequate THz reflection is caused by the conical tympanic membrane by simulation.

Two types of TOS were designed and fabricated (ATOS,ITOS), which indirectly demonstrate that the fabricated TOS can measure reflected THz pulses from practical tympanic membranes, through simulation and experiment using thin dielectric film and thin mouse skin.

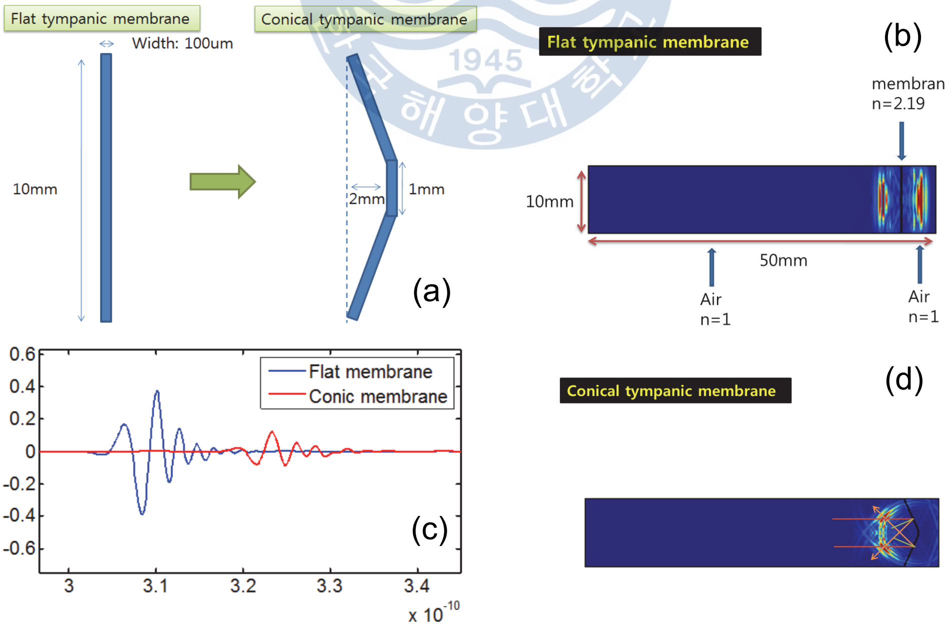

Figure 5-19 Reflection simulations from flat membrane and conic membrane.

7. Conclusion

A miniaturized optical fiber-coupled TES (THz endoscope) and TOS (THz otoscope) have been designed, fabricated, and characterized, and are excellent for the diagnosis of cancer and otitis media, respectively. *In-vivo* measurements of the human body which cannot be measured, such as with the side wall of the mouth and tongue, have been carried out using the manufactured TES, and the diagnostic ability for otitis media has been demonstrated by simulations and experiments with dielectric thin film and mouse skin used to modeled the tympanic membrane with FDTD and the manufactured TOS.

First, a fiber-coupled THz system, which is commonly used on TES and TOS, was described in detail. The relation between measured THz pulses and the dispersion of femtosecond laser pulse was described. The optimized incident angle and distance between the grating pair used to compensate the dispersive laser pulse passing through a 2-m-long optical fiber was determined by experiment.

In order to manufacture the TES, modularization and miniaturization are essential. The manufacturing processes of the PTES (prototype TES) with 20-mm diameter and 90-mm length have been described, and the modularization was demonstrated by PTES. All parts for the PTES were miniaturized, such as the Si lens, the optical lens part with fiber, and the semiconductor chip. The MTES (miniaturized TES) whose final size was 8 mm X 6 mm X 27 mm was fabricated and manufactured using miniaturized components. The propagation properties and spatial divergence of the MTES were investigated. The amplitude and spectrum bandwidth were reduced when the angle and distance of the Tx and Rx modules were large.

For the *in-vivo* measurement, the Tx and Rx modules of the MTES were fixed at an angle of 20 degrees on a custom-made mount, and the reflection distance between the Si lenses and sample was always 1.5 cm. In order to create the same experimental conditions, a 3-mm-thick and 15-mm-diameter Teflon plate was attached to the modules in the shape of a cap. The refractive indices and power absorptions of the side wall of the mouth and tongue, which cannot be measured, were reported using the fabricated MTES. The palm of a hand and water were measured in addition to the two *in-vivo* samples, and the measurements demonstrated that the MTES can distinguish not only each part of the human body, but also cancer.

The manufacturing methods of the SMTES (super miniaturized TES) were proposed to extend the versatility of the MTES. The fabricated MTES had separate Tx and Rx modules, which limited miniaturization. Therefore, to achieve super miniaturization, an integration method to unite the separate Tx and Rx modules into a single module has been used. The THz pulses were generated and detected by a TATT (twin antenna THz transceiver) using two photoconductive antennas on one LTG-GaAs substrate and a custom twin-core optical fiber. The SMTES with the TATT, to which the fast scanning method can be applied without an optical chopper was demonstrated. The SNR (signal to noise ratio) of the THz pulse measured by the SMTES was still low because of the large amount of noise caused by the bias voltage, So zero-voltage SMTES using LPDE (lateral photo-Dember effect) was suggested.

Finally, a TOS that can diagnose otitis media using technique of the MTES was fabricated and studied. The manufacturing processes of ATOS (angled TOS) and ITOS (interferometric TOS) were explained in detail. It was indirectly demonstrated that the fabricated TOS can measure reflected THz pulses from a practical tympanic membrane through simulations and experiments using thin dielectric film and thin mouse skin.

Reference

[1] Martin van Exter and D. Grischkowsky, "Optical and Electronic Properties of Doped Silicon from 0.1 to 2 THz", Appl. Phy. Lett., 56, 1694 (1990).

[2] Martin van Exter and D. Grischkowsky, "Carrier Dynamics of Electrons and Holes in Moderately-doped Silicon", Phys. Rev. B15, 41, 12140-9 (1990).

[3] Tae-In Jeon and D. Grischkowsky, "Nature of Conduction in Doped Silicon," Phys. Rev. Lett., 78, 1106 (1997)

[4] H. Harde, Soeren Keiding and D. Grischkowsky, "THz Commensurate Echoes: Periodic Rephasing of Molecular Transitions in Free Induction Decay", Phys. Rev. Lett., 66, 1834 (1991).

[5] Hai-Bo Liu, Yunqing Chen, Glenn J. Bastiaans, and X.-C. Zhang, "Detection and identification of explosive RDX by THz diffuse reflection spectroscopy", Opt. Express, 14, 1, 415 (2006).

[6] R. H. Clothier and N. Bourne, “Effects of THz exposure on human primary keratinocyte differentiation and viability,” J. Biol. Phys., 29, 179 (2003).

[7] M. R. Scarfì, M. Romanò, R. DI Pietro, O. Zeni, A. Doria, G.P. Gallerano, E. Giovenale, G. Messina, A. Lai, G. Campurra, D. Coniglio and M. D’Arienzo, “THz Exposure of Whole Blood for the Study of Biological Effects on Human Lymphocytes,” J. Biol. Phys., 29, 171 (2003).

[8] B. B. Hu and M. C. Nuss, "Imaging with terahertz waves", Opt. Lett. 20, 16, 1716 (1995).

[9] Y. U. Jeong, G. M. Kazakevitch, H. J. Cha, S. H. Park, and B. C. Lee, "Application of a wide-band compact FEL on THz imaging," Nucl. Instrum. and Methods in Phys. Res. A 543, 90 (2005)

[10] L. Young, V. V. Prabhu, E. W. Prohofsky, and G. S. Edwards, "Prediction of

modes with dominant base roll and propeller twist in B-DNA poly(dA)-poly(dT)", Phys. Rev. A 41, 7020 (1990).

[11] B. M. Fischer, M. Hoffmann, H. Helm, R. Wilk, F. Rutz, T. Klein-Ostmann, M. Koch, and P. U. Jepsen, "Terahertz time-domain spectroscopy and imaging of artificial RNA", Opt. Express 13, 5205 (2005).

[12] A. G. Markelz, A. Roitberg, and E. J. Heilweil, "Pulsed terahertz spectroscopy of DNA, bovine serum albumin and collagen between 0.1 and 2.0 THz", Chem. Phys. Lett. 320, 42 (2000).

[13] R. M. Woodward, V. P. Wallace, R. J. Pye, B. E. Cole, D. D. Arnone, E. H. Linfield, and M. Pepper, “Terahertz pulse imaging of ex vivo basal cell carcinoma,” J. Invest. Dermatol. 120, 72 (2003).

[14] A. J. Fitzgerald, V. P. Wallace, M. Jimenez-Linan, L. Bobrow, R. J. Pye, A. D. Purushotham, and D. D. Arnone, “Terahertz pulsed imaging of human breast tumors,” Radiology 239, 533 (2006).

[15] J.-H. Son, “Terahertz electromagnetic interactions with biological matter and their applications,” J. Appl. Phys. 105, 102033 (2009).

[16] S. J. Oh, J. Kang, I. Maeng, J.-S. Suh, Y.-M. Huh, S. Haam, and J.-H. Son, “Nanoparticle-enabled terahertz imaging for cancer diagnosis,” Opt. Express 17, 3469 (2009).

[17] E. Pickwell, B. E. Cole, A. J. Fitzgerald, M. Pepper, and V. PWallace, "In vivo study of human skin using pulsed terahertz radiation", Phys. Med. Biol., 49, 1595 (2004).

[18] R. W. McGowan, G. Gallot, and D. Grischkowsky, "Propagation of Ultra-Wideband, Short Pulses of THz Radiation through Sub-mm Diameter Circular Waveguides," Opt. Lett., 24, 1431 (1999).

[19] G. Gallot, S.P. Jamison, R.W. McGowan, D. Grischkowsky, "THz Waveguides," J. Opt. Soc. B., 17, 851 (2000).

[20] R. Mendis and D. Grischkowsky, "Plastic Ribbon THz Waveguides," J.Appl. Phys., 88, 4449 (2000).

[21] R. Mendis and D. Grischkowsky, "THz Interconnect with Low Loss and Low Group Velocity Dispersion," IEEE Microw. Wirel. Compon. Lett., 11, 444(2001).

[22] Tae-In Jeon and D. Grischkowsky, "Direct optoelectronic generation and detection of subps electrical pulses on sub-mm coaxial transmission lines," Appl. Phys. Lett., 85, 25, 6092 (2004).

[23] K. Wang, and D. M. Mittleman, “Metal wires for terahertz wave guiding,” Nature 432, 376 (2004).

[24] M. Mbonye, R. Mendis, and D. M. Mittleman, "A terahertz two-wire waveguide with low bending loss," Appl. Phys. Lett., 95, 233506 (2009).

[25] J. V. Rudd, and D. M. Mittleman, “Influence of substrate-lens design in terahertz time-domain spectroscopy,”J. Opt. Soc. Am. B 19, 319 (2002).

[26] S. A. Crooker, “Fiber-coupled antennas for ultrafast coherent terahertz spectroscopy in low temperatures and high magnetic fields,” Rev. Sci. Instrum. 73, 3258 (2002).

[27] C. Jördens, N. Krumbholz, T. Hasek, N. Vieweg, B. Scherger, L. Bahr, M. Mikulics, and M. Koch, “Fibrecoupled terahertz transceiver head,” Electron. Lett. 44, 1473(2008).

[28] A. Bartels, R. Cerna, C. Kistner, A. Thoma, F. Hudert, C. Janke, and T. Dekorsy, "Ultrafast time-domain spectroscopy based on high-speed asynchronous optical sampling," Rev. Sci. Instrum., 78, 035107 (2007).

[29] S. Kray, F. Spöler, T. Hellerer, and H. Kurz, "Electronically controlled coherent linear optical sampling for optical coherence tomography," Opt. Express, 18, 9976 (2010).

[30] Y. Kim and D.-S. Yee, "High-speed terahertz time-domain spectroscopy based on electronically controlled optical sampling," Opt. Lett., 35, 3715 (2010).

[31] G.-J. KIM, S.-G. JEON, J.-i. KIM, and Y.-S. JIN, "Terahertz Pulse Detection Using Rotary Optical Delay Line," Jpn. J. Appl. Phys., 46, 7332 (2007).

[32] D. Grischkowsky, S. Keiding, M. van Exter and Ch. Fattinger, "Far-Infrared Time-Domain Spectroscopy with Terahertz Beams of Dielectrics and Semiconductors", JOSA-B, 7, 2006 (1990).

[33] K. Sakai, "Terahertz Optoelectornics," Springer Verlag (2005).

[34] L. Duvillaret, F. Garet, J.-F. Roux, and J.-L. Coutaz, "Analytical Modeling and Optimization of Terahertz Time-Domain Spectroscopy Experiments Using Photoswitches as Antennas," JSTQE, 7, 615 (2001).

[35] M. T. Reiten and R. A. Cheville, "Effect of spherical aberration and surface waves on propagation of lens-coupled terahertz pulses," Opt. Lett., 30, 673 (2005).

[36] Y. B. Ji, E. S. Lee, S.-H. Kim, J-H. Son, and T.-I. Jeon, "A miniaturized fiber-coupled terahertz endoscope system," Opt. Express, 17, 17082 (2009).

[37] T.-I. Jeon, and D. Grischkowsky, “Characterization of optically dense, doped semiconductors by reflection THz time domain spectroscopy,” Appl. Phys. Lett., 72, 3032 (1998).

[38] S. A. Maier, S. R. Andrews, L. Martín-Moreno, and F. J. García-Vidal, “Terahertz surface plasmon-polariton propagation and focusing on periodically corrugated metal wires,” Phys. Rev. Lett., 97, 176805 (2006).

[39] C. Winnewisser, F. Lewen, and H. Helm, “Transmission characteristics of dichroic filters measured by THz time-domain spectroscopy,” Appl. Phys., A Mater. Sci. Process. 66, 593 (1998).

[40] V. P. Wallace, A. J. Fitzgerald, E. Pickwell, R. J. Pye, P. F. Taday, N. Flanagan, and T. Ha, “Terahertz pulsed spectroscopy of human Basal cell carcinoma,” Appl. Spectrosc., 60, 1127 (2006).

[41] E. Pickwell, and V. P. Wallace, “Biomedical applications of terahertz technology,” J. Phys. D. Appl. Phys. 39, 301 (2006).

[42] M. Tani, Z. Jiang and X.-C. Zhang, "Photoconductive terahertz Transceiver," Electron. Lett., 36, 804 (2000).

[43] M. Tani, M. Watanabe and K. Sakai, "Photoconductive twin dipole antennas for THz transceiver," Electron. Lett., 38, 5 (2008).

[44] X.-C. Zhang, and D. H. Auston, “Optoelectronic measurement of semiconductor surfaces and interfaces with femtosecond optics,” J. Appl. Phys. 71, 326 (1992).

[45] K. Liu, J. Xu, T. Yuan, and X.-C. Zhang, "Terahertz radiation from InAs induced by carrier diffusion and drift," Phys. Rev. B, 73, 155330 (2006).

[46] M. B. Johnston, D. M. Whittaker, A. Dowd, A. G. Davies, E. H. Linfield, X. Li, and D. A. Ritchie, “Generation of high-power terahertz pulses in a prism,” Opt. Lett., 27, 1935 (2002).

[47] G. Klatt, F. Hilser, W. Qiao, M. Beck, R. Gebs, A. Bartels, K. Huska, U. Lemmer, G. Bastian, M. Johnston, M. Fischer, J. Faist, and T. Dekorsy, "Terahertz emission from lateral photo-Dember currents," Opt. Express 18, 4939 (2010).

[48] G. Klatt, B. Surrer, D. Stephan, O. Schubert, M. Fischer, J. Faist, A. Leitenstorfer, R. Huber, and T. Dekorsy, "Photo-Dember terahertz emitter excited with an Er:fiber laser," Appl. Phys. Lett., 98, 021114 (2011).

[49] E. Pickwell and V. P. Wallace, "Biomedical applications of terahertz technology," J. Phys. D: Appl. Phys. 39. R301 (2006).

[50] S. Sy, S. Huang, Y.-X. Wang, J. Yu, A. T. Ahuja, Y.-t. Zhang and E. Pickwell," Phys. Med. Biol. 55, 7587 (2010).